



HAL
open science

Hole polarons in LaFeO_3 and

$\text{La}_{1-x}\text{Sr}_x\text{FeO}_{3-\delta}$:

Stability, trapping, mobility, effect of Sr concentration, and oxygen vacancies

Cintia Hartmann, Jérôme Laurencin, Grégory Geneste

► **To cite this version:**

Cintia Hartmann, Jérôme Laurencin, Grégory Geneste. Hole polarons in LaFeO_3 and $\text{La}_{1-x}\text{Sr}_x\text{FeO}_{3-\delta}$: *Stability, trapping, mobility, effect of Sr concentration, and oxygen vacancies*. 03990325

HAL Id: hal-03990325

<https://hal.science/hal-03990325v1>

Submitted on 15 Feb 2023

HAL is a multi-disciplinary open access archive for the deposit and dissemination of scientific research documents, whether they are published or not. The documents may come from teaching and research institutions in France or abroad, or from public or private research centers.

L'archive ouverte pluridisciplinaire **HAL**, est destinée au dépôt et à la diffusion de documents scientifiques de niveau recherche, publiés ou non, émanant des établissements d'enseignement et de recherche français ou étrangers, des laboratoires publics ou privés.

Hole polarons in LaFeO_3 and $\text{La}_{1-x}\text{Sr}_x\text{FeO}_{3-\delta}$: stability, trapping, mobility, effect of Sr concentration and oxygen vacancies.

Cintia Hartmann^{1,2,*}, Jérôme Laurencin³, and Grégory Geneste^{1,2†}

¹ *CEA, DAM, DIF, F-91297 Arpajon, France*

² *Université Paris-Saclay, CEA, Laboratoire Matière en Conditions Extrêmes,
91680 Bruyères-le-Châtel, France and*

³ *Univ. Grenoble Alpes - CEA/LITEN,
17 rue des Martyrs, 38054, Grenoble, France*

(Dated: February 14, 2023)

Abstract

The stability, trapping and mobility of electron holes are investigated in lanthanum ferrite LaFeO_3 , and in $\text{La}_{1-x}\text{Sr}_x\text{FeO}_{3-\delta}$ ($x \approx 0.1, 0.4$ and 0.6) by hybrid-density-functional and density-functional-theory+ U calculations. In pure LaFeO_3 , the electron hole is more stable under a localized (polaronic) form than under a delocalized form, the energy difference (self-trapping energy) lie between ≈ -0.3 and -0.4 eV. This self-trapped hole polaron is not strictly localized on a single Fe atom: instead, it occupies a quantum state made of a $3d$ orbital of a Fe atom, strongly hybridized with $2p$ orbitals of four neighboring oxygen. The hole polaron is thus localized on 5 atoms (among which one single Fe), which can be described as the Fe^{3+} oxidation into Fe^{4+} . Electron hole transport results from the combination of onsite-reorientations and hoppings, with energy barriers estimated at ≈ 0.01 - 0.20 eV and 0.3 - 0.4 eV, respectively. The aliovalent substitution of lanthanum by strontium in LaFeO_3 , induces the presence of localized electron holes, preserving the insulating character of $\text{La}_{1-x}\text{Sr}_x\text{FeO}_3$, regardless of the studied Sr concentration. The formation energy of the oxygen vacancy in $\text{La}_{1-x}\text{Sr}_x\text{FeO}_3$ ($x \approx 0.1$ and 0.4) is estimated at $\approx +0.8$ eV. This value is here successfully used to quantify the evolution of defect concentration as a function of the oxygen partial pressure.

I. INTRODUCTION

Solid Oxide Cells (SOCs) are high-temperature electrochemical devices working typically at around 1073 K. This system is used to convert electrical energy into dihydrogen gas when operating in electrolysis or SOEC (Solid Oxide Electrolyzer Cell) mode ($\text{H}_2\text{O} \rightarrow \text{H}_2 + \frac{1}{2}\text{O}_2$). Thanks to its reversibility, the same device can also be used to convert gas into electrical power via the reverse reaction $\text{H}_2 + \frac{1}{2}\text{O}_2 \rightarrow \text{H}_2\text{O}$: it then works in fuel cell or SOFC (Solid Oxide Fuel Cell) mode. In SOEC mode, the energy is stored by synthesizing gas, while in the SOFC mode, gas is re-converted into electricity. Basically, SOCs consist of a dense electrolyte which is an ionic *conductor* but an electronic *insulator* sandwiched between two porous electrodes exhibiting an electric and ionic conductivity. In standard SOCs, the electrolyte is made of Yttrium-doped Stabilized Zirconia (YSZ). The hydrogen electrode is a cermet made of Nickel and YSZ, while the oxygen electrode is made of Lanthanum Strontium Cobalt Ferrite (LSCF). The latter compound is a mixed ionic and electronic conductor at high temperature.¹ It is a perovskite oxide that contains two transition metals, cobalt and iron, on its B site, while the A site is occupied by lanthanum or strontium. In this system, substitution of La by Sr plays the role of an acceptor doping and thus introduces holes in the compound. In contrast, the possibility of creating vacancies on the oxygen sublattice (thus removing oxygen) plays the role of a donor process, and thus introduces electrons in the system. The efficiency and durability of SOCs depend on the material physical and chemical properties of each cell component and, hence, a deep understanding of the physics at the microscopic scale should help to design electrolytes and electrodes with improved properties.

In this work, we investigate some properties of the compound Lanthanum Strontium Ferrite $\text{La}_{1-x}\text{Sr}_x\text{FeO}_{3-\delta}$ (LSF), which may be considered as a simplified model for LSCF. It can also be used as an oxygen electrode material of SOCs.² The parent compound LaFeO_3 (LF) is a G-type antiferromagnetic (AFM) electronic insulator with the perovskite structure, that crystallizes in the orthorhombic $Pnma$ space group (Glazer notation $a^-a^-b^+$). LSF exhibits with varying x a wide range of physical properties, such as optical absorption,^{3,4} antiferromagnetism,⁵ charge-ordering^{6,7} or electro-catalytic activity,⁸⁻¹⁰ e.g. for water splitting and hydrogen production, through an efficient Oxygen Evolution Reaction (OER).¹¹ In this work, we will mainly focus on the electronic and electrical behavior of LSF.

As mentioned above, Sr substitution in LaFeO₃ in the place of La is an acceptor doping which, in the absence of charge compensation by oxygen vacancies, induces the presence of electron holes in the system. Experimental studies suggest that these holes should be rather spatially localized – inducing semiconducting behavior – on a very large range of x , before transition towards a metallic behavior for $x \approx 1$.^{12,13} These holes are associated with electronic states within the bandgap, and are supposed to be at least partly localized in $3d$ orbitals of Fe atoms. They can thus be described as a Fe mixed valence with an oxidation of Fe³⁺ into Fe⁴⁺. Experiments however have shown that the hole states should also be partly hybridized with oxygen $2p$ orbitals.^{14,15}

Despite a rather large number of studies performed on LSF, some questions remain open concerning the morphology of the electron holes and their localization. Besides, the evolution of this-localization with x as well as the hole mobility and interaction with Sr impurities and with oxygen vacancies is still not precisely understood.

Furthermore, in this study a special focus lies on the formation of oxygen vacancies and the dependence of oxygen deficiency on pressure and temperature. In fact, the concentration of oxygen vacancies at equilibrium C_V plays a key role on the electrode response. Indeed, at zero current density or under cathodic polarization (i.e. in fuel cell mode), it has been shown that the reaction mechanism is controlled by the so-called ‘bulk path’. For this reaction pathway, the oxygen vacancies are transported from the electrolyte interface to the electrode surface where they are consumed by the reaction of oxygen incorporation. The electrode polarization resistance at open circuit potential can be then approximated by the following relation¹⁶:

$$R_p \propto \frac{1}{C_V}, \tag{1}$$

From this relation, it appears that the polarization resistance decreases with increasing the concentration of oxygen vacancies at equilibrium. Besides, it is worth noting that the strong depletion of oxygen vacancies under anodic polarization (i.e. in electrolysis mode) could trigger a transition in the reaction mechanism from the ‘bulk’ to the ‘surface’ path.^{17,18} This evolution could also be involved in a phase decomposition arising upon operation in electrolysis mode.¹⁹ Therefore, the precise knowledge of the oxygen vacancy concentration is essential for a precise assessment of the electrode efficiency

In this work, these issues have been addressed by using Hybrid Density-Functional and

Density-Functional-Theory+ U calculations. The present article is organized as follows: after describing the computational background in Sec. II, we investigate the properties of self-trapped holes in pure LaFeO₃, i.e. self-trapping and hopping processes, in Sec. III. The properties of holes in La_{1-x}Sr_xFeO₃, in particular their interaction with Sr impurities, are presented in Sec. IV. The formation of oxygen vacancies in LSF is finally investigated in sec. V, and the computed data are used as inputs in a defect model that allows describing the defect concentration as a function of temperature and oxygen partial pressure. Last but not least, in the subsection VD, the hole conductivity is investigated under different conditions.

II. DENSITY-FUNCTIONAL THEORY CALCULATIONS

The calculations have been carried out in the frame of the spin-polarized Kohn-Sham Density-Functional Theory (DFT) calculations using the ABINIT code.²⁰ The Generalized Gradient Approximation was employed with the Perdew, Burke, and Ernzerhof functional (GGA-PBE).²¹ The Projector-Augmented Wave (PAW) method was used, with PAW datasets taken from the JTH table.²²⁻²⁴ For a better treatment of correlated electrons, the Hubbard U correction was applied on the d states of Fe. Two different values of U were evaluated, $U=3$ eV and $U=4$ eV. As shown in Tab. I, we found that both values lead to the correct stabilization of the G -type AFM phase in LF, when compared to the other AFM orders (A -type and C -type) and to the ferromagnetic (FM) one and lead to similar structural and magnetic properties. In rhombohedral LSF with $x \approx 0.4$, the G -type AFM order was also tested and found more stable than the FM state (Tab. I). However, since a slightly better concordance with experimental results for the band gap was obtained with $U=3$ eV (Tab. II), this value was mostly retained in the DFT+ U calculations.

It is worth noting that similar values have been employed by several authors. For instance, Ritzmann *et al.* used a value of $U=4.3$ eV for LSF, which was derived from unrestricted Hartree-Fock calculations on electrostatically embedded Fe₂O₃.²⁵ In a second article about LSCF, the same authors used a value of $U=4$ eV for both Fe and Co.²⁶ On the other hand, Das *et al.* had chosen the U value based on a comparison between experimental and calculated structural and magnetic properties by testing U values in the range of 0.2 and 4 eV. In order to identify a U parameter adapted for different oxidation states (between Fe²⁺

and Fe^{4+}), their study was carried out on LSF, LF and LS compounds and they found an optimal value equal to $U=3$ eV.²⁷

All our calculations were performed using a plane-wave cut-off energy of 20 Hartrees (Ha). The SCF cycle was stopped when the differences of maximal forces reached twice successively the tolerance criterion of 1×10^{-6} Ha/bohr, or when the difference of maximal forces are smaller than 0.02 times the maximum force. The electronic occupancies were determined with the Gaussian method using a smearing parameter of 0.0025 Ha. For the structural optimizations, the Broyden-Fletcher-Goldfarb-Shanno (BFGS) minimization, as implemented in ABINIT, was used and minimization converged until the atomic forces were at least below 2×10^{-4} Ha/bohr (≈ 0.01 eV/Å).

The computations on $\text{La}_{1-x}\text{Sr}_x\text{FeO}_3$ have been performed for three different Sr concentrations: $x \approx 0.1, 0.4$ and 0.6 . For each concentration, the calculations were carried out using the corresponding experimental crystal structure, as reported in Ref. [28].

The crystal structure of LSF depends on its strontium concentration x ²⁸:

- for $0 \leq x \leq 0.2$ (low Sr content), LSF has the structure of its parent compound LF (orthorhombic, $Pnma$, Glazer notation $a^-a^-b^+$);
- for $0.4 \leq x \leq 0.7$, LSF adopts a rhombohedral structure with space group $R\bar{3}c$ (Glazer notation $a^-a^-a^-$);
- for $0.8 \leq x \leq 1.0$, LSF is cubic (space group $Pm\bar{3}m$, Glazer notation $a^0a^0a^0$).

The cell parameters were fixed to the experimental ones, avoiding lattice expansion due to the application of the GGA-PBE functional.

For pure LaFeO_3 , the 20-atom orthorhombic unit cell was used with a $4 \times 4 \times 3$ k -point mesh to sample the First Brillouin Zone. For the orthorhombic region of LSF (low Sr content), we constructed a $2 \times 2 \times 2$ supercell (in terms of the 20-atom unit cell), thus containing 160 atoms. The First Brillouin Zone associated with this supercell was sampled by a $2 \times 2 \times 2$ k -point-mesh. A $2 \times 2 \times 1$ (120 atoms) supercell was used for the rhombohedral region, and k -point sampling was performed on a $3 \times 3 \times 2$ mesh. For the calculations of electronic density of states (DOS), the k -point-mesh was doubled along the three directions.

In the LSF compound, the random distribution of the Sr atoms within the La sublattice is modeled using Special Quasi-random Structures (SQS) generated with the Monte Carlo

TABLE I: Ground state energies (eV) for LF and LSF($x \approx 0.4$) for different magnetic orders: ferromagnetic (FM), anti-ferromagnetic (AFM) of type A , C and G , calculated using experimental lattice parameters. In each case, the energies are relative to the most stable magnetic state (G-type AFM).

	FM	A-AFM	C-AFM	G-AFM
LaFeO₃				
U=3 eV	1.139	0.717	0.316	0.0
U=4 eV	0.927	0.637	0.282	0.0
LSF ($x \approx 0.4$)				
U=3 eV	0.787	-	-	0.0
U=4 eV	0.080	-	-	0.0

TABLE II: Iron-oxygen distances and angles, Kohn-Sham bandgap E_g , and iron spin magnetic moment M_{Fe} in LaFeO₃, calculated in GGA+ U assuming the G-type AFM magnetic order.

	Fe-O _z (Å)	Fe-O _{xy} (Å)	Fe-O-Fe (°)	E_g (eV)	M_{Fe} (μ_B)
Expt.	2.009 ^a	2.002 ^a	157.257 ^a	2.0 ^b	4.6 ^c
		2.009	155.662 ^a	2.1 ^d	
U=3 eV	2.013	2.010	155.145	2.035	4.05*
		2.017	154.575		4.65**
U=4 eV	2.013	2.010	155.172	2.393	4.11*
		2.016	154.523		

^a Ref.²⁸,

^b Ref.¹⁵,

^c Ref.²⁹,

^d Ref.³⁰

* Atomic occupations are integrated values in PAW spheres. ** Extrapolations of occupancies outside the PAW-sphere.

SQS code implemented in the Theoretical Automated Toolkit.^{31,32}

However, even if the GGA+ U functional perfectly succeeds in describing the localized holes induced by the presence of Sr in LaFeO₃ at large Sr concentration, it failed to correctly simulate the self-trapped hole polarons at small or vanishing Sr concentration. In literature,

Hybrid Density-Functional calculations have been successfully used for the study of polarons in transition metal oxides.^{33,34,35,36,37,38,39} Therefore, the Heyd-Scuseria-Ernzerhof hybrid functional (HSE06), as implemented in the VASP code, was also employed for calculations of hole polarons in pure LaFeO₃ or in La_{1-x}Sr_xFeO₃ with $x=0.1$.⁴⁰⁻⁴² Owing to their computational cost, these calculations were performed using the Γ point only to sample the Brillouin Zone associated with the 160-atom supercell. A finer mesh of $2 \times 2 \times 1$ was used in one case to check the validity of the result. Structural optimizations with VASP were also performed using a tolerance of 0.01 eV/Å on the maximal forces. The first calculations performed in this work with GGA+ U in LSF, as well as the calculations of Zhu *et al.*⁴³ on LF, revealed that hole polarons in this system have a particular (quasi-planar) form: they are centered on an Fe atom but also extend on four neighboring oxygens. Thus, there are three possibilities for the configuration of a self-trapped hole polaron, according to the crystallographic plane along which it lies, and thus, its simulation requires to initially select the oxygen atoms involved in the polaronic state. For that, the polaron is "prepared" by shortening "manually" the distance between Fe and the four oxygens involved in the polaron by about 0.15-0.25 Å (and not for the two others). Then, a self-consistent single-point GGA+ U calculation is performed on this frozen geometry: it provides wave functions that are used as inputs of the HSE06 calculation, for which the geometry is eventually relaxed. The final HSE06 result, with the visualization of the charge density associated with the polaronic state, allows controlling that the state, which has been reached corresponds to the targeted one. Thanks to this method, we can obtain the three possible orientations of the polarons, which are centered on the same Fe atom.

III. HOLES POLARONS IN LAFEO₃

Before examining the complex LSF supercells, we focus on pure LaFeO₃ and scrutinize whether it is possible or not to stabilize holes under a *polaronic form* in this oxide, and how these holes can jump from a site to another.

A. Electronic structure of LaFeO₃

The total electronic densities of states (DOS) and orbital-projected densities of states (pDOS) of LaFeO₃ are presented on Fig.1 (a). Our results for the electronic structure of LaFeO₃ are similar to already published works (e.g. Ref. 44): Indeed, LaFeO₃ is an electronic insulator in which the Fe are in charge state +3 (Fe³⁺), in a high-spin (HS) electronic state ($3d_{\uparrow}^5 3d_{\downarrow}^0$, or $3d_{\uparrow}^0 3d_{\downarrow}^5$), leading theoretically to 5 μ_B (i.e five parallel spins). In our calculations, the spin magnetic moment has been estimated to 4.0-4.1 μ_B from the populations of 3d electrons inside PAW spheres (Tab. I). The order of the magnetic moments is *G*-type AFM, and thus the DOS given in Fig. 1 (a) is symmetric in the spin up and down channels, such that the net spin magnetic moment over the unit cell is zero. The band gap between the valence band (VB) and conduction band (CB) is about 2.035 eV, in good agreement with experimental results.¹⁵

It has been confirmed that the conduction band mainly consists of empty Fe 3d orbitals (slightly mixed to O 2p orbitals). Due to crystal field splitting, these unoccupied Fe 3d orbitals are split into three-fold t_{2g} states and two-fold e_g states, separated from each other by 1.2 eV, in agreement with X-ray Absorption Spectroscopy (XAS) measurements.^{15,45} Below the Fermi level, the DOS has a more complex character. If we would neglect interactions between Fe 3d electrons and electrons from the surrounding, we would expect a shift of the occupied Fe 3d states of about $U=3$ eV to lower energy, conserving the crystal field splitting. However interactions with oxygen lead to a mixed Fe 3d and O 2p valence band character. Fixing the origin of energies as the top of the VB, three different regions can be identified within the valence band:

- Low-energy region (bottom of the VB, between ≈ -6.6 eV and -5.35 eV) where the Fe 3d orbitals dominate,
- Intermediate-energy region (center of the VB, between ≈ -5.35 eV and -0.95 eV) in which the main contribution comes from the O 2p orbitals,
- High-energy region (top of the VB, between ≈ -0.95 eV and 0 eV) composed of strongly hybridized Fe 3d and O 2p states.

Due to the mixed Fe 3d - O 2p character of the states near the valence band maximum (VBM), LaFeO₃ can be considered as an intermediate charge transfer/Mott insulator. The

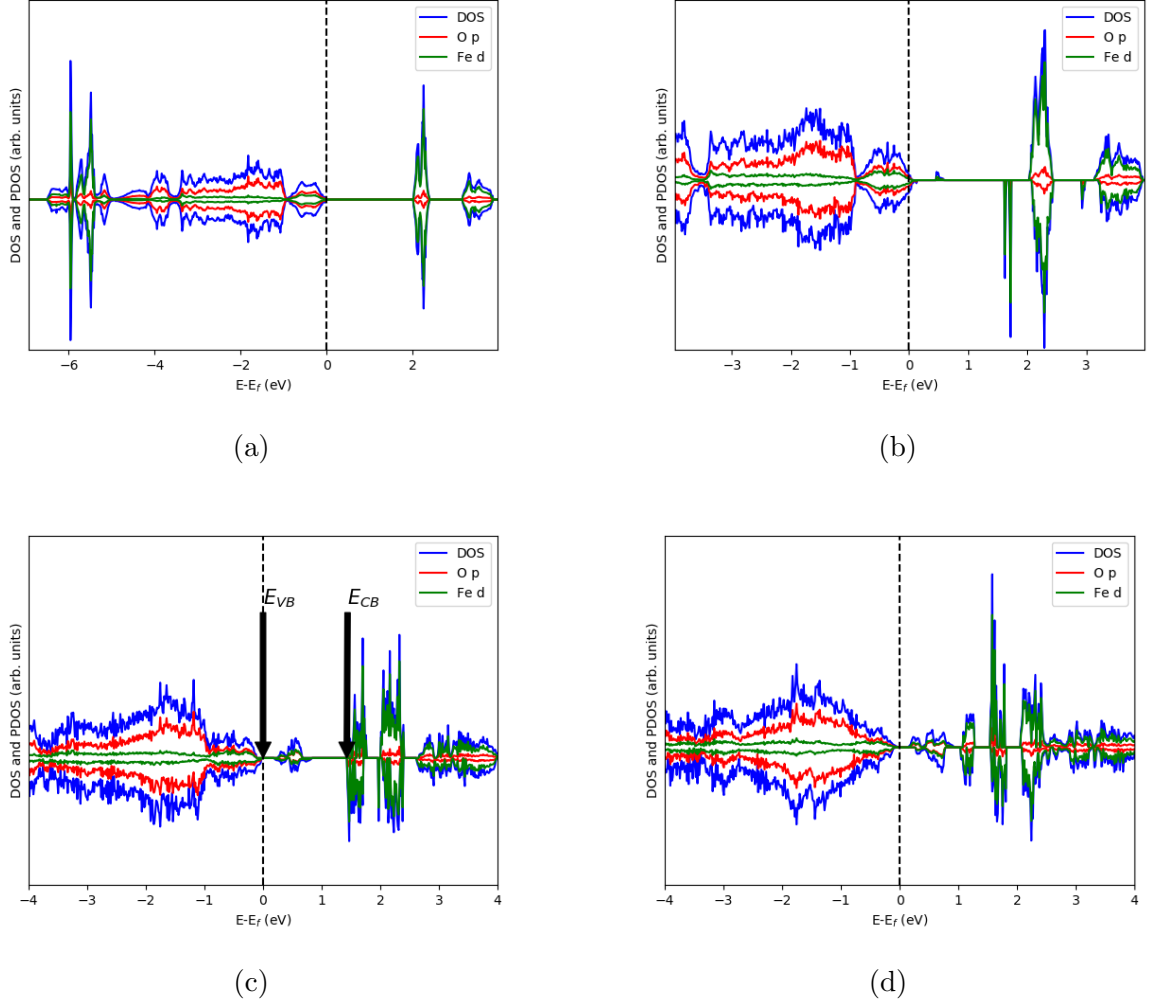


FIG. 1: Total and projected density of states obtained by GGA+ U for (a) LF, (b) LSF with $x \approx 0.1$, (c) $x \approx 0.4$ and (d) $x \approx 0.6$ imposing a G-type AFM arrangement of the Fe magnetic moments. The energy scale is relative to the Fermi energy ($E_f=0$) and the DOS for spin-up (resp. spin-down) electrons are represented with positive (resp. negative) values. The total DOS is displayed with a blue line and PDOS of O $2p$ states and Fe $3d$ states with a red and green line, respectively. The systems are insulating, except LSF with $x \approx 0.1$, found to be slightly metallic (which is however an artefact of GGA+ U).

nature of the orbitals near the VBM – Fe $3d$ hybridized with O $2p$ – can be used to predict the nature of the holes in LaFeO₃.

B. Stability of self-trapped hole polarons in LaFeO₃

The mixed Fe $3d$ - O $2p$ character of the electronic states at the VBM suggests that holes in LaFeO₃, that are obtained by emptying these VBM states, should be partly localized on Fe (in $3d$ orbitals) and on O (in $2p$ orbitals). However, our attempts to simulate stable self-trapped hole polarons in pure LaFeO₃ using GGA+ U revealed unsuccessful: either the hole evolved to a state delocalized throughout the supercell, or the polaronic configuration was found to have a larger energy than the delocalized one. Using GGA+ U functional, a slightly negative self-trapping energy was only obtained under the condition to add a supplementary Hubbard correction on the p orbitals of oxygen, in agreement with the simulations by Wheeler *et al.*⁴⁶

However, in a recent work, Zhu *et al.*⁴³ used the HSE06 functional to simulate self-trapped hole polarons in LaFeO₃, and obtained a rather large negative self-trapping energy of -0.42 eV. Following these authors, we therefore used this functional (Fig. 2), and as expected, we obtained a stable hole polaron similar to the one described by Zhu *et al.*⁴³ Moreover, as expected from the pDOS of bulk LaFeO₃, it can be seen in Fig. 3 that the hole is localized on both: a Fe atom, and 4 neighboring oxygen atoms. Its state thus appears as a molecular orbital, corresponding to a linear combination of one Fe $3d$ orbital and four O $2p$ orbitals. From this analysis, it appears that the hole is not rigorously a *small* polaron since it is localized, with significant density of probability, on 5 atoms rather than on a single one (Fig. 3(i)). Note that the four oxygen involved belong to the same plane within the perovskite network. Moreover, as expected the hole state is now localized within the bandgap, at about ≈ 1.4 eV from the VBM, and the system recovers the density of states of an insulator (Fig. 2 (a)), in contrast with the (less stable) configurations in which the hole is delocalized (Fig. 2 (b)).

The hole polaron in this first configuration appears as lying along the equatorial plane of the orthorhombic structure, which corresponds to the (xy) plane on Fig. 3 (i). Here, we denote by x , y and z the cartesian axis of the orthorhombic cell, while we denote by a , b and c those of the perovskite network for the pseudo-cubic directions. The apical direction is chosen to be $z=c$, while the a and b axis are turned by 45° with respect to the x and y ones, see Fig. 3. The obtained self-trapping energy is -0.30 eV for a k -point sampling restricted to Γ . Using the special point $(1/2\ 1/2\ 1/2)$, the computed self-trapping energy is increased to

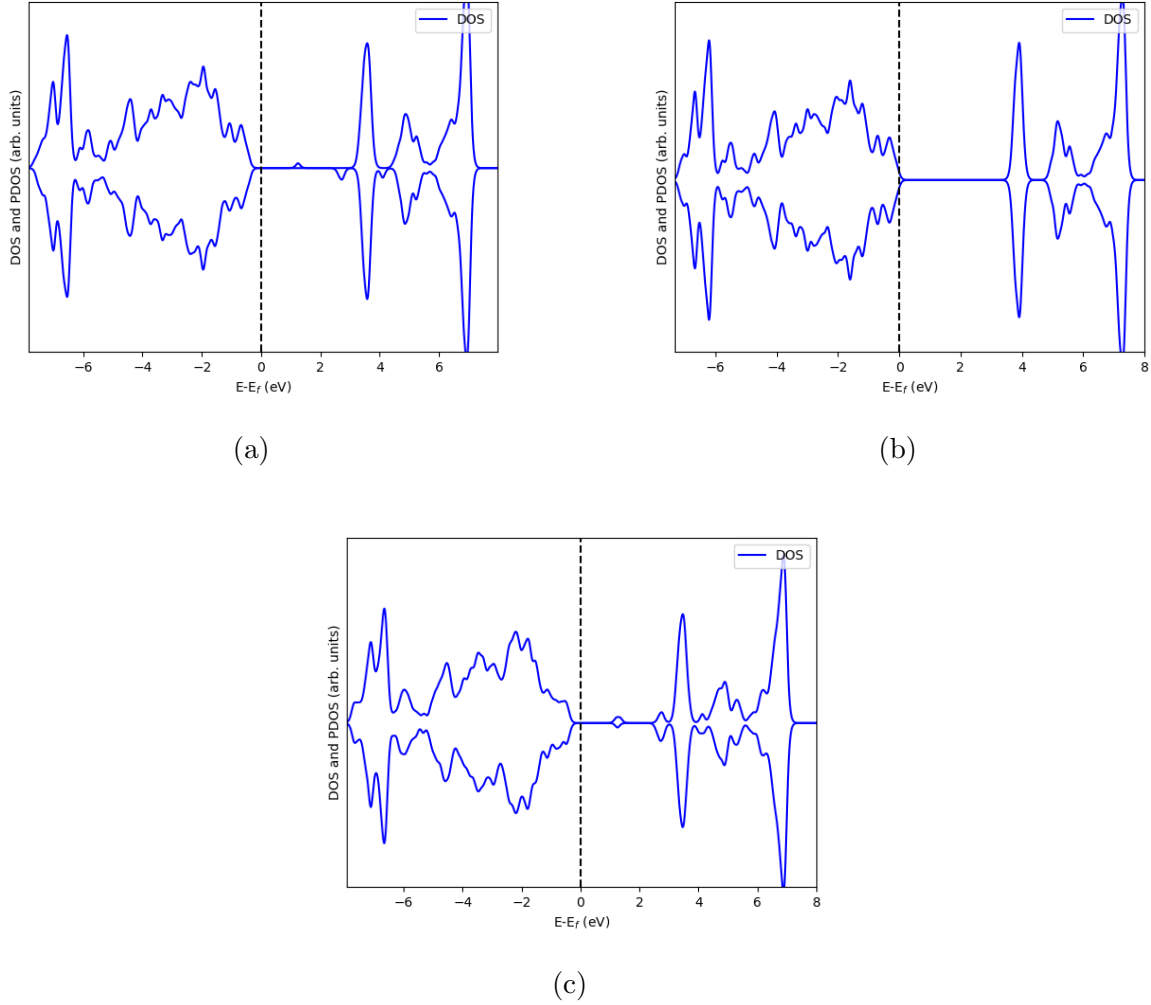


FIG. 2: Electronic densities of states of (a) the LF supercell with a self-trapped hole polaron, (b) the same supercell with a delocalized hole, and (c) the LSF supercell with $x \approx 0.1$, as obtained using the HSE06 functional. The Fermi energy is set at 0 eV.

-0.46 eV (close to the result of Zhu *et al*⁴³) while a value of -0.36 eV is reached with a finer $2 \times 2 \times 1$ k-point mesh. In this state, the Fe atom thus appears as oxidized, and the Fe-O bond lengths – between the 5 atoms involved in the polaron – within the equatorial plane are shortened to 1.90 and 1.86 Å (versus 2.01 and 2.02 Å at Fe³⁺ ion at 2NN position), see Fig. 3 (iv), (v). The distance between the iron of the polaron and the two nearest oxygen that do not belong to the polaron is both 2.05 Å. The Fe atom, on which the polaron is centered, has a lower spin magnetic moment ($\approx 3.5 \mu_B$) with respect to the other Fe atoms of the supercell (≈ 4.0 - $4.1 \mu_B$), reflecting the loss of d electrons and thus a more oxidized

state.

In a second step, we also simulated the self-trapped hole polaron lying along the two other possible crystallographic planes, (bc) and (ac) , the three states obtained being not equivalent in the orthorhombic crystal structure of LaFeO_3 , see Fig. 3 (ii), (iii). Nevertheless, the obtained self-trapping energies (-0.29 and -0.25 eV respectively) are close to the previous one (Tab. III). The most stable configuration corresponds to the hole polaron lying within the equatorial plane $(ab)=(xy)$. In these two configurations, the Fe-O distances between the 5 atoms involved in the polaron are respectively ≈ 1.91 - 1.92 and 1.85 - 1.86 Å for the polaron being along (bc) and (ac) planes. Moreover, the distances between the iron of the polaron and the two nearest oxygen that do not belong to the polaron are ≈ 2.05 - 2.06 Å which are very close to the values mentioned in the case where the polaron lies along (ab) .

For the polaron lying along (ac) , a slightly more stable polaronic configuration has been found with a self-trapping energy = -0.28 eV. In this case Fe-O distances of 1.93 - 1.94 Å have been found between Fe and the four oxygen of the polaron, while the distance between Fe and the two oxygen, which are not involved in the polaron, has been estimated to 2.02 Å (we call this state $(ac)'$).

TABLE III: Self-trapping energies for the three possible configurations of the self-trapped hole polaron in LaFeO_3 , as obtained from HSE06 calculations with a sampling of the supercell Brillouin Zone reduced to Γ .

Configuration (plane of the polaron)	(ab)	(bc)	(ac)	$(ac)'$
Self-trapping energy (eV)	-0.30	-0.29	-0.25	-0.28

C. Mobility of self-trapped holes polarons in LaFeO_3

We now turn to the mobility of the self-trapped hole polarons in LaFeO_3 . Two kinds of motions can be considered: (i) onsite reorientations of the hole polaron on its site; (ii) hoppings from one site into a next one.

For each mechanism, we construct between the initial (\mathbf{R}_i) and final (\mathbf{R}_f) configurations, which have been previously optimized, a set of 9 intermediate configurations by a linear interpolation of the atomic positions, $\mathbf{R}(\lambda) = (1 - \lambda)\mathbf{R}_i + \lambda\mathbf{R}_f$, $\lambda = 0.1, 0.2 \dots 0.9$. For

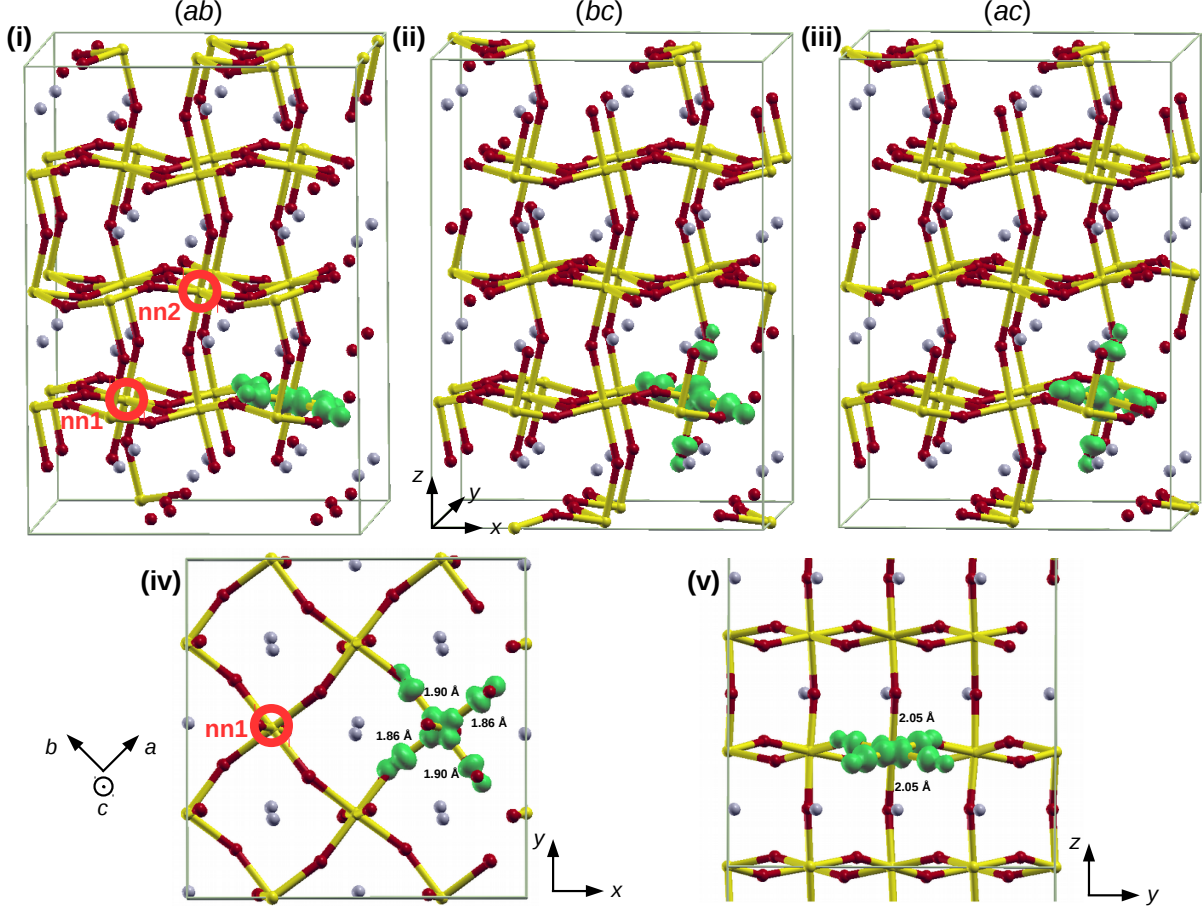


FIG. 3: (i),(ii) and (iii): Isosurfaces of electron charge density (the isovalue is $0.05 \text{ e}/\text{\AA}^3$) of the three possible configurations of the self-trapped hole polaron in the orthorhombic crystal LaFeO_3 . z is the apical direction. (iv), (v): two other views of configuration (ab) where the hole polaron lies along the equatorial plane. Fe-O distances within the polaron are indicated on panel (iv).

each of these intermediate configurations, the energy has been calculated using the HSE06 functional (single-point calculations). This procedure provides an upper bound to the energy barrier for reorientation/hopping of the hole polarons, since the path obtained through this linear interpolation of the atomic positions is not relaxed to the minimum energy path.

1. Onsite reorientations

Fig. 4 displays the energy profiles for the three onsite-reorientations of the self-trapped hole polaron, and the corresponding energy barriers. The two reorientations $(ab) \Leftrightarrow (bc)$ and

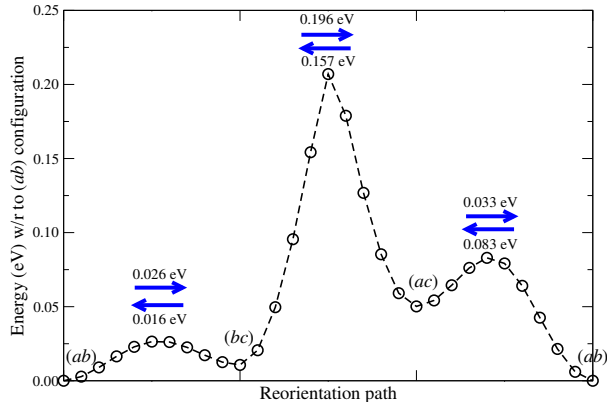


FIG. 4: Energy profile for the three onsite-reorientations of the self-trapped hole polaron, from (ab) to (bc) , from (bc) to (ac) and from (ac) to (ab) , with the corresponding energy barriers. The energy of (ab) is taken as reference.

$(ac) \Leftrightarrow (ab)$ are associated with rather small barriers of ≈ 0.02 - 0.08 eV. They correspond to rotations of the polaron around an axis that belongs to the equatorial plane. However, the third one, $(bc) \Leftrightarrow (ac)$ is associated with larger barriers of ≈ 0.16 - 0.20 eV. This latter process corresponds to the rotation of the polaron around the apical axis.

2. Hoppings

For hole polaron having a well-defined spin, a single hopping mechanism within the G -type AFM structure of LaFeO_3 is only possible with motions towards a 2nd-neighbor Fe atom, i.e. along a $[110]$ -type pseudocubic direction. Nevertheless, because of the orthorhombic symmetry, there is a large number of possible hopping paths for the self-trapped hole. Besides, we have selected three other possible configurations, corresponding to the polaron lying on a 2nd-neighbor Fe atom, and calculated the energy profiles for the 9 hoppings going from each of these three configurations onto each of the three states on the reference Fe (here again, the paths are constructed according to a simple linear interpolation between the atomic positions of the initial and final configurations). The energy profiles associated with these 9 hopping paths are shown on Fig. 5. They exhibit energy barriers typically between 0.3 and 0.4 eV.

All of the obtained energy profiles exhibit an angular shape in the saddle point configuration, suggesting an abrupt change in the polaron state at that point: indeed, the polaron is mostly localized on the initial Fe along the first part of the path, while it is mostly localized on the final Fe along the second part of the path. In the neighborhood of the saddle point (i.e. highest energy along the path), the Fe involved in the polaron is either the initial one, the final one, or both of them, depending on the case, as indicated by the plot of the spin magnetic moments of the two Fe involved in the hopping along the different paths (Fig. 6).

However, because the activation energy was determined using linear interpolation between initial and final atomic positions, the minimum energy path for hopping might be smoother, with reduced activation barriers. Moreover, no information about the electronic coupling in each of the saddle point configurations can be inferred from the present analysis. It is thus difficult to determine whether these hopping mechanisms take place in an adiabatic or in a non-adiabatic regime. Therefore, at this state, further investigations are still necessary to better specify the type of hopping mechanism.

Activation energies derived from conductivity measurements performed at low temperature have been estimated to around ≈ 0.3 eV.^{47, 48, 49} Even if these experimental data are slightly below our DFT predictions, they are still in satisfying agreement. It can be noticed that Wang *et al.* observed a change in the activation energy with temperature for LSF ($0.1 \leq x \leq 0.2$).⁴⁹ Indeed, the activation energy was found equal to 0.3 eV in the low temperature range (300-573 K) and then decreased to around 0.1-0.2 eV for higher temperatures (573-873 K). Similarly, the activation energy fitted in a temperature range of 1073-1273 K by Kobayashi *et al.* leads to a value of 0.113 eV.⁵⁰ Tai *et al.* found an activation energy for LSF ($x = 0.2$) of around 0.09 eV in a temperature range between 400-800°C.⁵¹ In addition, Patrakeev *et al.* determined activation energies with values close to zero for LSF ($x \leq 0.5$) between 650-950°C.⁵² Our low temperature DFT calculations were performed with an antiferromagnetic order consistent with the experimental low temperature magnetic structure. Therefore, the hopping was calculated between second nearest neighbors sites with same spin orientation. However, we speculate that at higher temperature (above the Néel temperature), the hopping between the first nearest neighbor sites might become possible. This mechanism could change the activation energy related to coincidence configuration between nearest neighbor sites. The aforementioned explanation could be at the origin of the low activation energy reported at high temperature but still needs to be verified. Experimentally

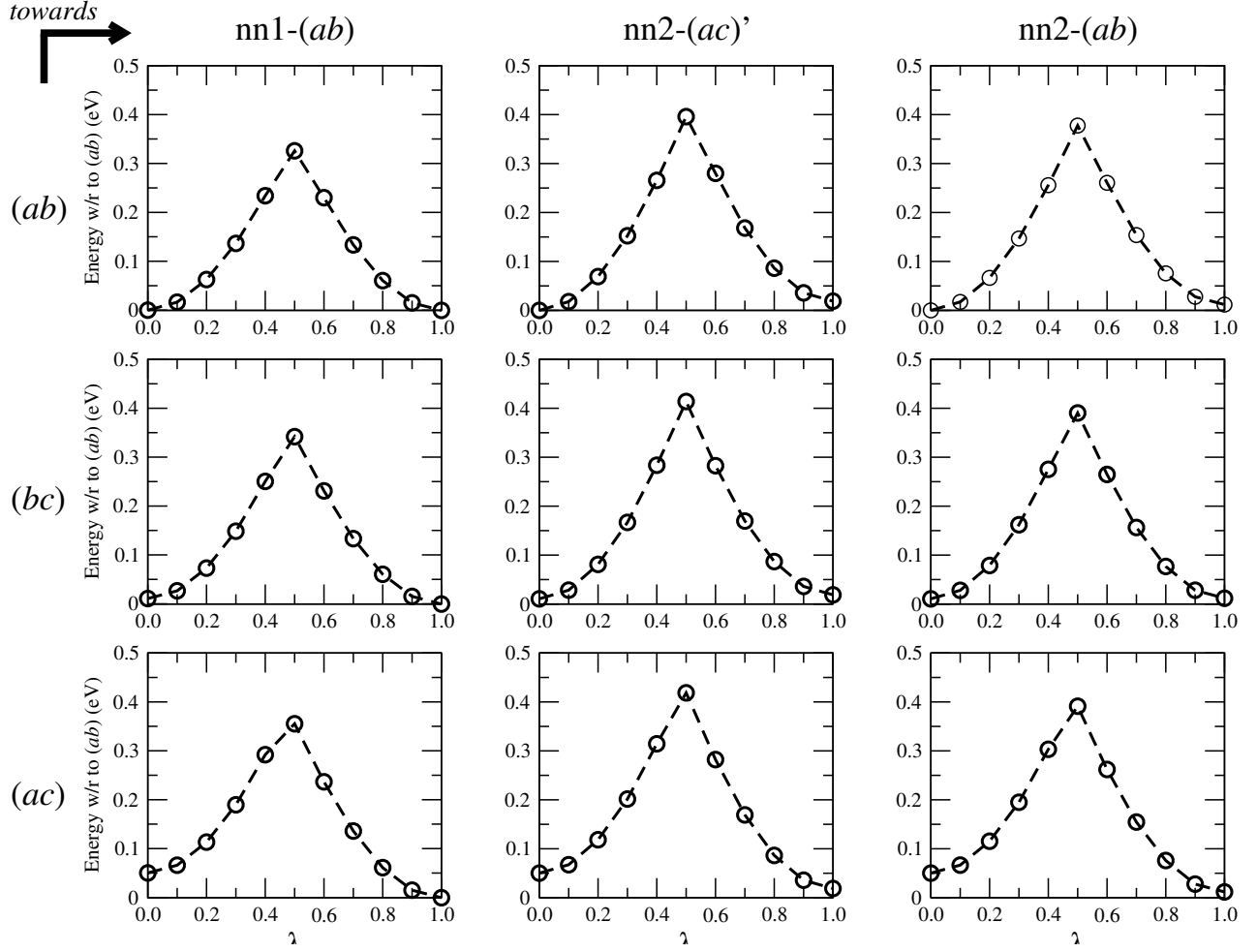


FIG. 5: Energy profile for nine hopping paths of the self-trapped hole polaron, from (ab), (bc), and (ac) onto two nearest-neighbor sites called nn1 and nn2, associated with three states of the polaron, see Fig. 3.

it has been found that the Néel temperature in LSF decreases from around 750 K for $x=0$, to approximately 400K for $x=0.3$.⁵³ For $x=0.1$, the Néel temperature has been estimated to approximately 600 K.⁵⁴

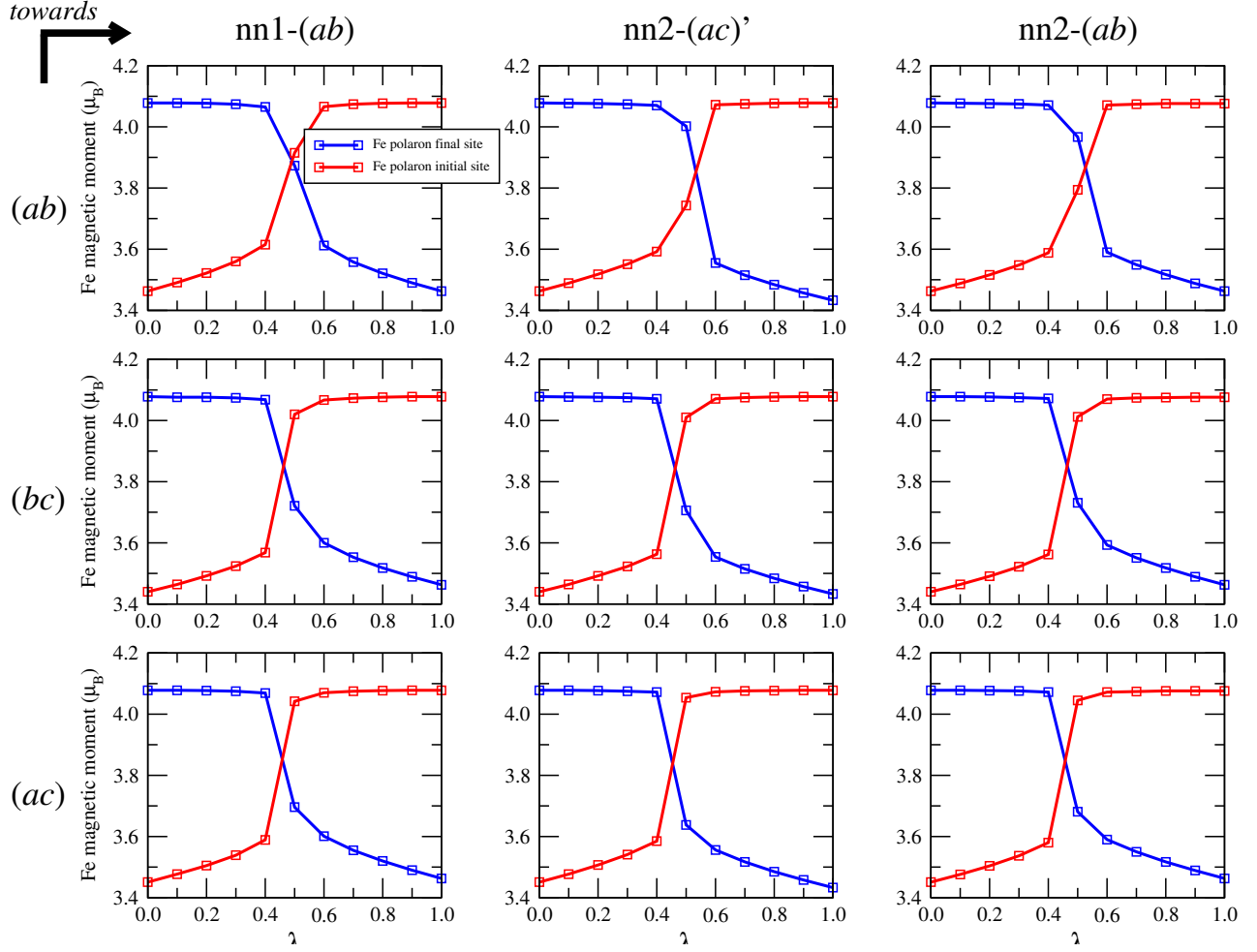


FIG. 6: Spin magnetic moment on the two Fe involved in the nine polaronic hopping of Fig. 5. The initial and final values (≈ 4.08 and $3.43\text{-}3.46 \mu_B$) respectively correspond to Fe^{3+} and Fe^{4+} .

IV. HOLES IN $\text{La}_{1-x}\text{Sr}_x\text{FeO}_3$

A. Low Sr concentration: $\text{La}_{1-x}\text{Sr}_x\text{FeO}_3$, $x=0.1$

1. Description with GGA+U

We now turn to LSF with a Sr concentration close to $x = 0.1$, at which LSF keeps the orthorhombic structure than pure LaFeO_3 . The corresponding DOS and pDOS, as obtained from GGA+U, are shown in Fig. 1 (b). First, it can be noticed that although the DOS partially loses its symmetry between the up and down spin channels, due to the presence

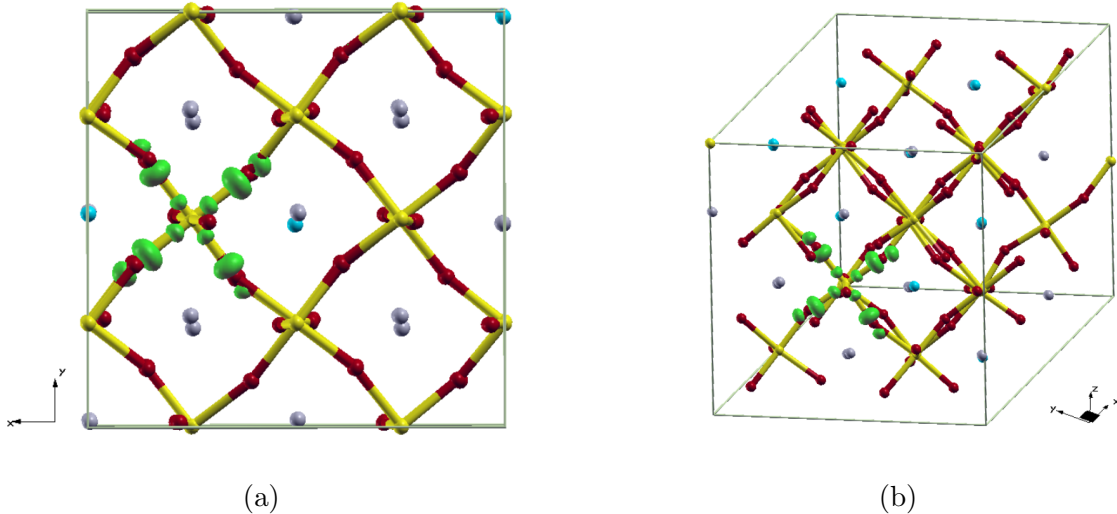


FIG. 7: Isosurfaces (20 % of the maximal value) of the probability amplitude of the wave-functions associated to the hole states in LSF for (a) $x \approx 0.1$ and (b) $x \approx 0.6$.

♣

of disordered Sr impurities, the net magnetic moment remains close to zero, preserving the AFM character of the structures.

As already mentioned, substituting La by Sr (acceptor doping) leads to the creation of electron holes, corresponding to states, which are emptied near the VBM. Here, the GGA+ U calculation have shown that LSF with $x \approx 0.1$ presents a configuration combining localized and delocalized electron holes. Indeed, it has been found that part of the empty states remain at the VBM, corresponding to delocalized states. While the other part forms a narrow band within the band gap, which suggests that they should be spatially localized: the Fermi level thus falls just below the VBM within GGA+ U , so that the system possesses a metallic character.

This simultaneous formation of delocalized and localized hole states would lead to a partial metallic behaviour, for which however no experimental evidence exists. In fact, experimental measurements show, for $x = 0.1$, that conduction is governed by a polaron hopping mechanism.⁴⁷ Le Wang *et al.* calculated the one-electron DOS using the hybrid B3LYP functional with an embedded cluster method, and found partially delocalized and localized states at low Sr concentrations. They attributed this feature to a too large Gaussian broadening parameter in their calculations rather than a partial metallic structure.¹² Nonetheless in the present DFT+ U calculations the Gaussian smearing parameter has been

chosen sufficiently small to avoid such a numerical artifact.

Here again, these electron holes are formed by strongly mixed Fe 3d-O 2p orbitals emanating from the upper VB, as anticipated from the DOS of pure LF, see Fig. 7 (a).

A substitution rate of $x \approx 0.1$ in LSF corresponds to three Sr impurities in the supercell and hence to the formation of three electron holes (one per Sr impurity). According to the GGA+ U simulations, two of them are spatially delocalized and are formed at the VBM, while the third hole state is spatially localized and lies detached from the VB at around 0.5 eV from the VBM. The probability amplitude of the wavefunction associated to the localized hole state reveals that the hole is similar to the one obtained in pure LaFeO₃, i.e. centered on an iron ion, with a spatial extension expanding over four of the surrounding oxygen ions, within a (100)-type plane. The iron on which this hole is centered (formally Fe⁴⁺) has a reduced magnetic moment of around 3.41 μ_B , while the others (Fe³⁺) have magnetic moments of about 4.0 μ_B . As explained above, the reduced magnetic moment can be thus interpreted as an iron of higher oxidation state, i.e. formally Fe⁴⁺. The presence of Fe⁴⁺ induces a division in the DOS of the unoccupied e_g and t_{2g} orbitals associated to Fe³⁺ and Fe⁴⁺ that can be observed in Fig. 1 (b). The fact that unoccupied Fe⁴⁺ 3d states move to lower energy might be explained with a lowered repulsion between electrons in Fe⁴⁺ as it contains one electron less compared to Fe³⁺.

Note that the shape of the electron hole and the associated distortion appears naturally after structural optimization starting from initially ideal crystallographic positions.

2. Description with HSE06

The existence of delocalized hole states in GGA+ U may be questioned regarding both the experimental results and the previous results obtained for the hole polaron in pure LaFeO₃, that we described as localized (self-trapped) using the HSE06 functional. Thus, we performed a new structural optimization of the supercell with $x \approx 0.1$, using the HSE06 functional. As expected in this case, the three holes, are spatially localized, forming a band of empty states within the gap, separated from the (fully occupied) VBM by approximately ≈ 1.6 eV. The system is thus obtained as insulating (Fig. 2 (c)). Iso-surfaces of these three hole states are displayed on Fig. 8. From this analysis, it appears that the HSE06 functional could be more adapted for DFT calculations on LSF for small Sr concentrations.

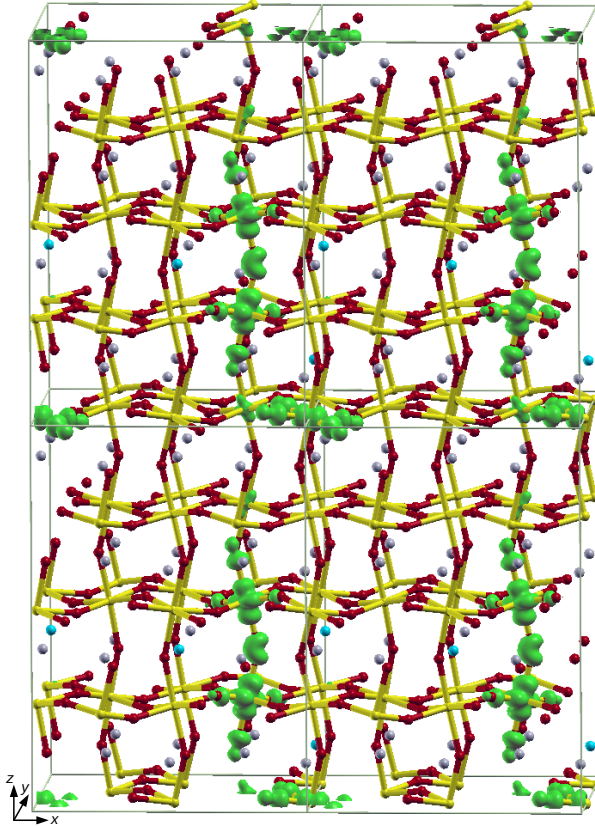


FIG. 8: Configuration of $\text{La}_{1-x}\text{Sr}_x\text{FeO}_3$ with $x \approx 0.1$, with isosurfaces (the isovalue is $0.05 \text{ e}/\text{\AA}^3$) of the three hole states, as obtained from the HSE06 structural optimization. The three holes are localized and close to the Sr impurities (blue circles). The supercell is doubled twice along x and z for a better view of the hole states.

3. Hole trapping by Sr impurities

We now examine whether holes preferentially localize in the neighborhood of Sr ions, as a consequence of the lower oxidation state of the substituent. Compared to La^{3+} , the Sr^{2+} ions act indeed like negative charges, which are expected to attract the positively charged holes. In the $\text{GGA}+U$ calculation, we observed that the localized hole is spontaneously placed on the diagonal between two Sr^{2+} ions, see Fig. 7 (a). In the HSE06 calculation, all the localized holes have either one or two Sr as first neighbor on the La/Sr sublattice (Fig. 8).

In order to quantify the *trapping energy* of the localized hole polaron near a Sr, we reoptimized, using the HSE06 functional, the present supercell with only one Sr, and positioned the hole polaron successively on two sites: for the three possible orientations, the first hole

was placed near Sr (Pos1) whereas the second one was put far away from Sr (Pos2) in the supercell (Tab. IV). It has been found, that the most stable configuration corresponds to the hole polaron being positioned in first neighbor from Sr, within the (ab) plane. For the polaron being far from Sr, the energy lies within 0.04-0.10 eV above the energy of the most stable configuration, suggesting a moderate trapping effect. However, the two configurations with the hole polaron close to Sr (Pos1) and lying along the (bc) and (ac) planes have energies within the same range. A small trapping energy ($\approx -0.03 / -0.04$ eV) is in fact observed for the polaron lying along the (ab) and (bc) orientations, but not along (ac) . The six configurations are shown on Fig. 9.

TABLE IV: Energies (in eV) of the configurations with one Sr and its associated hole, in six different relative configurations corresponding to two sites (Pos1 and Pos2, see main text) and the three possible orientations (ab) , (bc) and (ac) . The energies are relative to the most stable one. The configurations are displayed on Fig. 9.

Polaronic site	Pos1	Pos1	Pos1	Pos2	Pos2	Pos2
Polaronic plane	(ab)	(bc)	(ac)	(ab)	(bc)	(ac)
Energy (eV)	0.0	0.040	0.103	0.044	0.071	0.098

B. Large Sr concentration: $\text{La}_{1-x}\text{Sr}_x\text{FeO}_3$, $x \approx 0.4$ and 0.6

At larger Sr concentration ($x \gtrsim 0.4$), the GGA+ U calculation successfully describes all the electron holes as spatially localized, forming a band of empty states within the bandgap, which becomes more pronounced and broad. For $x \approx 0.4$ and $x \approx 0.6$, all hole states are thus localized so that LSF regains its insulating character: the DOSs present a clear band gap between the (occupied) VB and the (unoccupied) hole state band, see Fig. 1 (c) and (d). At the same time, the division of unoccupied Fe $3d$ states is still detected and is proportional to the Fe^{4+} and Fe^{3+} concentrations, respectively. In order to verify that this result does not depend on the specific SQS arrangement of Sr on A sites, we simulated the DOS for different configurations at fixed Sr concentration ($x \approx 0.4$). For all these configurations we obtained a similar result. Note that the Fe^{4+} higher oxidation state is accompanied with a decrease of the Fe-O bond length (Fig. 10). This DFT prediction is consistent with the

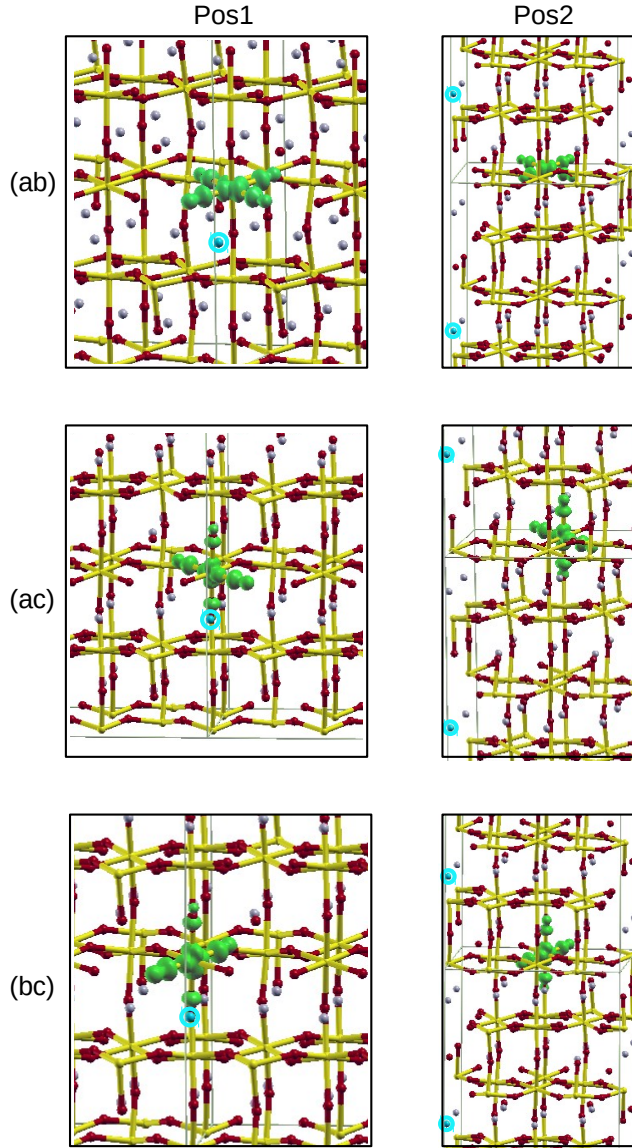


FIG. 9: The isosurfaces (the isovalue is $0.05 \text{ e}/\text{\AA}^3$) of six configurations with one Sr impurity and its associated hole, localized on two sites (Pos1: close to Sr; Pos2: far from Sr) and along the three possible orientations: (ab) , (ac) and (bc) . The Sr atom is in blue, and surrounded with a light blue circle for better visibility.

experimental evolution of the unit cell volume with the Sr content in LSF, which has been observed to decrease with the Sr concentration.¹²

To the best of our knowledge, the present results differ from most of the previously published DFT+ U calculations where the VB crosses the Fermi level even at intermediate Sr concentrations, leading to a conductive character.^{25,55,27} It is worth noting that the published

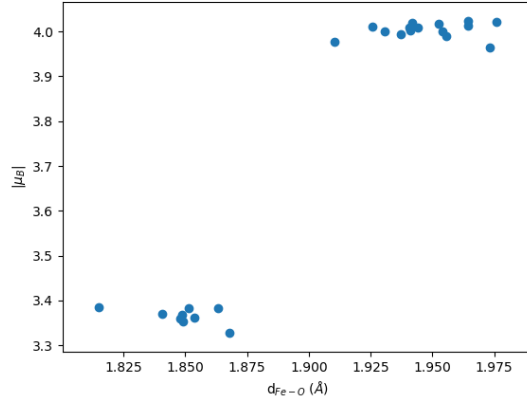


FIG. 10: Spin magnetic moment on Fe (μ_B) as a function of the shortest Fe-O bond length (d_{Fe-O}) in LSF ($x \approx 0.4$).

pDOS from Ref. [55] and the pDOS, averaged over the sites containing the same element of Ref. [56,25] possess a common feature. When examining carefully the pDOS for the occupied Fe 3d states, these states are mainly presented in the spin up pDOS. This common characteristic suggests an alignment of magnetic moments mainly in a ferromagnetic order. In fact, we calculated the DOS for the ferromagnetic order and found as well a crossing of the VB through the Fermi level (Fig. 11). This result shows that an accurate prediction of the electronic properties must rely on a correct description of the magnetic order with DFT+ U in LSF. This statement is important if the DFT+ U calculation aims to investigate the material properties with applications as electronic and ionic conductors, such as LSF and LSCF. It can be noticed in the DFT+ U ($U=3$ eV) DOS of LSF ($x=0.5$) in Ref. [27,57], the correct anti-ferromagnetic order in the rhombohedral structure has been used. Nevertheless, no localized states appear within the band gap and the VB crosses the Fermi level. This could maybe be a consequence of other DFT-settings or the choice of the ordered arrangement in the supercell with alternating La-O and Sr-O layers leading to a supercell of higher symmetry ($R\bar{3}2$ instead of $R\bar{3}c$).

Recently Shen *et al.* published a DFT+ U ($U=3$ eV) DOS with the correct (AFM) magnetic order and where hole localization has been observed.¹¹ The authors found that the DOSs are in good agreement with their experimental results. They were able to correlate an enhancement of the experimental OER with the formation Fe^{4+} states. However, as this article mainly focuses on the experimental investigations, details of these calculations are

unfortunately not available and the precision of the numerical resolution is not sufficient to be able to capture the fine electronic structure, such as the split in unoccupied Fe^{4+} and Fe^{3+} $3d$ states. Furthermore, it is hard to distinguish whether crossing through the Fermi level occurs or not.

In the present work, it is worth noting that the DOSs capture the main experimental results, corresponding to the appearance of hole states within the band gap.^{58,15,12,11} The proportionality between Sr concentration and the number of created hole states as well as the continuous broadening of the associated band is well reproduced. Furthermore, our results confirm the mixed Fe $3d$ - O $2p$ character of the hole states emanating from the upper valence band. Besides, they provide additional information about where hole states are created in space and how the shape of the hole states changes with increasing Sr concentration. LSF is thus found to have an insulating character regardless of the Sr concentrations studied (from $x = 0.1$ to 0.6) and in the perfect compound (LF), holes localize under the form of self-trapped polarons.

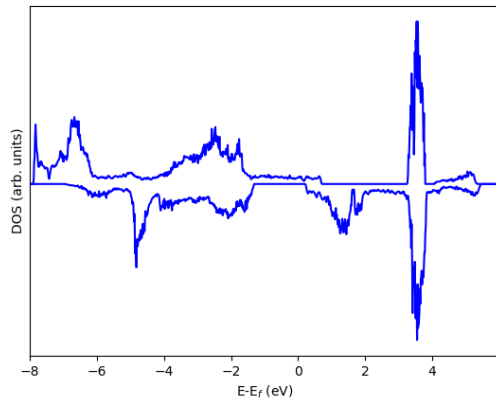


FIG. 11: Total density of states (DOS) for LSF ($x \approx 0.4$) imposing a ferromagnetic arrangement of magnetic moments. The system is metallic.

V. OXYGEN VACANCY FORMATION

The electrical conduction properties of LSF are closely related to its defect chemistry.

In LSF, the ionic charge difference due to the substitution of La^{3+} by Sr^{2+} has to be balanced. As previously highlighted, this charge compensation can be realized by the formation

of electron holes. This process is accompanied by the formation of irons with higher oxidation state (Fe^{4+} instead of Fe^{3+}). In turn, the charge compensation can also be achieved by the consumption of Fe^{4+} into Fe^{3+} with the creation of *oxygen vacancies* in LSF and the production of oxygen in the gas phase.

A. The oxygen vacancy in $\text{La}_{1-x}\text{Sr}_x\text{FeO}_3$, $x \approx 0.1$ and $x \approx 0.4$: GGA+ U calculations.

The formation energies E_f of oxygen vacancies in LSF with the Sr concentration $x \approx 0.1$ and $x \approx 0.4$ have been calculated by GGA+ U calculations by removing one oxygen atom from the corresponding supercells, according to

$$E_f = E_v + \frac{1}{2}E_{O_2} - E_p, \quad (2)$$

where E_p , E_v and E_{O_2} are respectively the total energies for the perfect supercell, the supercell with the oxygen vacancy and the isolated O_2 molecule. The three cases have been structurally optimized with respect to atomic positions.

1. Preferential sites for the oxygen vacancy

The orthorhombic and rhombohedral supercells here considered for LSF contain 96 and 72 oxygen sites, respectively. It is obviously not possible to calculate the vacancy formation energy for each of these 168 oxygen sites. Therefore, it is not known where oxygen vacancies will preferentially form in the crystal. In other words, the question arise as to whether some oxygen sites can promote the oxygen vacancy formation depending on their local environment. In Sec IV A 3, it has been observed that for $x \approx 0.1$, the electron hole localization takes place on the diagonal between two Sr^{2+} ions, which was explained using a simplified electrostatic approach. With a similar argumentation, it can be speculated that the oxygen vacancies, being twice positively charged, might also be attracted by Sr^{2+} ions.

In order to determine the effect of Sr on the position of the oxygen vacancy, an artificial system has been considered. This system consists of LF with a rhombohedral structure containing one strontium ion and where for nearest, second nearest and third nearest neighbors oxygen vacancy formation was simulated. The environment of the supercell is single

positively charged in order to isolate the effect of the defect interaction between Sr^{2+} and $V_{\text{O}}^{\bullet\bullet}$. The most stable location for the formation of an oxygen vacancy was found to be at the nearest neighbor position, as expected (see Tab. V). This statement, confirms the attraction between the oxygen vacancy and the Sr impurity meaning that oxygen vacancies may preferentially localize close to Sr atoms.

TABLE V: Artificial rhombohedral LF containing one Sr impurity and one oxygen vacancy. The supercell is charged +1 by a uniform background to ensure that there is no electronic defect. Sr-O Bond length r_{SrO} before structural optimization and energy of the system in (eV) with oxygen vacancy at nearest (1), second (2) and third (3) nearest neighbor (NN) position (the energies are referred to the most stable one).

	r_{SrO} [Å]	E [eV]
1NN	2.46	0.0
2NN	2.83	0.05
3NN	3.14	0.17

For the calculation of oxygen vacancy formation energies in LSF for $x \approx 0.1$ and $x \approx 0.4$, the supercells possess several Sr defects. In such supercells, finding the most favorable site for a positively charged defect remains difficult as the optimal position depend now also on the electrostatic potential created by all the Sr defects together. As a guide to find the optimal oxygen vacancy formation sites, we can use the result of the calculation without oxygen vacancy of the uncharged supercells for $x \approx 0.1$ and $x \approx 0.4$. In these calculations, as previously highlighted, the charge difference created by the Sr impurities are compensated by holes. These holes are singly positively charged. When considering only the interaction between holes and Sr defects, the holes should localize at electrostatically favorable sites with respect to the Sr impurities. Therefore, one could expect, that when introducing an oxygen vacancy in this system, it might occupy a site close to which the positively charged electron holes were previously located and which thus might also constitute an electrostatically favorable position for the doubly positively charged oxygen vacancies. In other words, the oxygen vacancy in $\text{La}_{1-x}\text{Sr}_x\text{FeO}_{3-\delta}$ may also localize at the same place as holes in $\text{La}_{1-x}\text{Sr}_x\text{FeO}_3$.

2. $La_{1-x}Sr_xFeO_{3-\delta}$, $x = 0$.

We first investigate the formation of the oxygen vacancy in pure $LaFeO_3$ (LF). In the orthorhombic structure of LF (space group $Pnma$), there are two non-equivalent oxygen usually denoted as "apical" and "equatorial". Both sites have been tested. Moreover, due to the absence of Sr impurity, the oxygen vacancy formation in pure LF releases two electrons that come to reduce two Fe^{3+} into Fe^{2+} . For the two sites, close and large values have been found for the formation energy: +4.50 eV (equatorial) and +4.48 eV (apical). In each case, the two electrons released by the vacancy are localized on the two nearest-neighbor iron atoms.

3. $La_{1-x}Sr_xFeO_{3-\delta}$, $x \approx 0.1$.

We now consider the orthorhombic supercell with $x \approx 0.1$, and remove one oxygen atom from the computed supercell. In this case, eight sites are tested, based on the previous GGA+ U results on the same supercell without vacancy, considering, as detailed above, that the oxygen atoms that have lost part of their electrons in this former case are probably the most favorable candidates for the vacancy sites. The Integrated Projected Density of States (IPDOS) can be used to assess in which extent an oxygen contributes to a hole state in the former calculation, even though the precision of IPDOS is unfortunately very limited. In Tab. VI, the contribution of the IPDOS to the localized hole state for 8 different oxygen is given as well as the oxygen formation energies. Oxygen with identification number 1-5 are bound to the Fe ion on which the hole is centered. The first of the four oxygen lie in the (xy) (equatorial) plane, while the fifth lies on the axis perpendicular to the plane. Although the contribution of the fifth oxygen is zero, visualization of the probability amplitude of the associated hole states shows a slight contribution but which is below the precision of the IPDOS.

For $x \approx 0.1$, the formation energies of the oxygen vacancy in each of the eight sites are given in Tab. VI: they are all positive, indicating that the oxygen incorporation (resp. ex-corporation) reaction in LSF is exothermic (resp. endothermic). The most favorable formation energy is 0.87 eV. It can be observed that the higher the contribution of an oxygen to the hole state, the lower is its oxygen vacancy formation energy. This result

TABLE VI: For $x \approx 0.1$, Integrated Projected Density Of State (IPDOS) on oxygen atoms in the supercell without vacancy, and energies before ($E_{f,1step}$) and relaxation after atomic positions ($E_{f,relaxed}$), in eV.

Oxygen ID	IPDOS	$E_{f,1step}$	$E_{f,relaxed}$
1	0.08	2.320	0.871
2	0.07	2.394	0.884
3	0.05	2.431	0.935
4	0.05	2.521	0.988
5	0.00	2.688	1.050
6	0.00	2.995	1.316
7	0.00	3.086	1.282
8	0.00	3.086	1.347

confirms that in the present case, the choice of the vacancy site based on the hole sites is correct.

4. $La_{1-x}Sr_xFeO_{3-\delta}$, $x \approx 0.4-0.6$.

We now consider the rhombohedral supercell with $x \approx 0.4$ from which one oxygen atom has been removed: ten sites are chosen based on the previous results on the same supercell without vacancy.

The contribution to localized hole states and formation energies for $x \approx 0.4$, before ($E_{f,1step}$) and after relaxation of the atomic positions ($E_{f,relaxed}$), are given in Tab. VII. The first step consists in removing an oxygen atom, i.e. breaking its chemical bonds and redistributing the electron density. Then, in a second step, the energy can be further minimized by relaxing the atomic positions, as previously done for $x \approx 0.1$. For both concentrations, $x \approx 0.1$ and $x \approx 0.4$, the atomic relaxation decreases significantly the cost of vacancy formation. For $x \approx 0.1$, the two formation energies ($E_{f,1step}$ and $E_{f,relaxed}$) follow a similar trend in IPDOS, for $x \approx 0.4$ only the formation energy after the first step exhibits this correlation. In this latter case ($x \approx 0.4$), the created local pressure after removal of an oxygen might be very different and depend on a more complex mechanism than the simplified electro-

static explanation given above so that atoms lose the correlation with IPDOS during atomic relaxation. Here again, the formation energies are positive and typically found around 1 eV.

TABLE VII: For $x \approx 0.4$, Integrated Projected Density Of State (IPDOS) on oxygen atoms in the supercell without vacancy, and energies before ($E_{f,1step}$) and after relaxation of the atomic positions ($E_{f,relaxed}$), in eV.

Oxygen ID	IPDOS	$E_{f,1step}$	$E_{f,relaxed}$
1	0.09	2.624	0.962
2	0.09	2.718	1.193
3	0.07	2.846	1.343
4	0.06	2.846	1.191
5	0.05	2.877	0.994
6	0.01	3.048	0.902
7	0.01	3.350	1.079
8	0.01	3.449	0.908
9	0.01	3.499	0.809
10	0.01	3.521	1.000

In addition to the vacancy formation energy for $x \approx 0.4$, the oxygen vacancy formation energy for $x \approx 0.6$ has been calculated at three oxygen sites. On average, the value obtained at this concentration is smaller than at lower concentration.

5. Oxygen vacancy formation energy as a function of Sr content

The oxygen vacancy formation energies as a function of Strontium content are shown in Fig. 12.

In the studied Sr concentration range, all vacancy formation energies are positive. It means that removing an oxygen atom from $\text{La}_{1-x}\text{Sr}_x\text{FeO}_3$ is an endothermic process, and that the (reverse) reaction of oxygen insertion is exothermic. In pure LaFeO_3 the formation energy of an oxygen vacancy is the highest with a value of ≈ 4.5 eV. Even a small increase of Sr content from $x=0.0$ to 0.1, creates a big jump of around 3.5 eV down to a lower value. This decrease in formation energy can quantitatively be explained since the redistribution of the

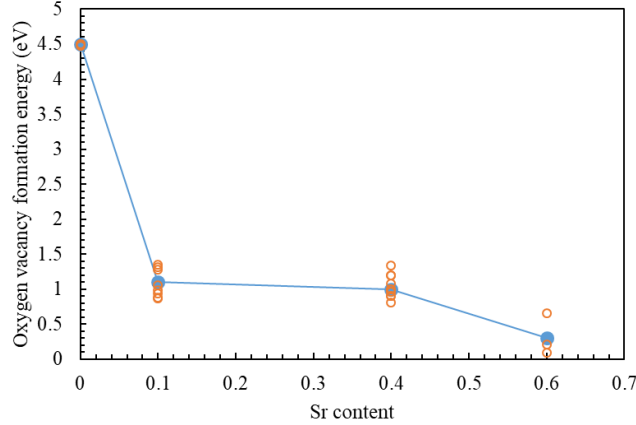


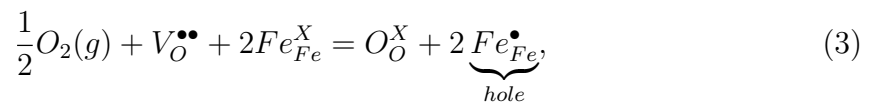
FIG. 12: Oxygen vacancy formation energies (in eV) as a function of Sr content. Open circles correspond to the values obtained for the different studied configurations and full circles to the mean formation energy at a given Sr content.

two liberated electrons on unoccupied e_g orbitals in Fe^{4+} is energetically less expensive than occupying an already single occupied t_{2g} state in Fe^{3+} . For $x \approx 0.1$ and 0.4 the formation energy is about 1 eV, in good agreement with the experimental data of Mizusaki *et al.*⁵⁹ By increasing the Sr-content to $x \approx 0.6$, DFT calculations result in a further decrease of the formation energy (~ 0.3 eV), although experimentally the formation energy is suggested to remain at around 1 eV.

B. Defect model

The oxygen vacancy concentration δ at a given temperature T and partial oxygen pressure P_{O_2} depends on the equilibrium between the electron holes and oxygen vacancy formation. In order to determine this equilibrium, the defect model used by Mizusaki *et al.* is now used.⁵⁹ According to the authors, the main defect mechanisms can be summarized by the following two reactions expressed in Kröger-Vink notations:

- Insertion of oxygen into a charged oxygen vacancy:



- Creation of an electron/hole pair:

$$2Fe_{Fe}^X = \underbrace{Fe'_{Fe}}_{electron} + \underbrace{Fe^{\bullet}_{Fe}}_{hole}. \quad (4)$$

Eq. 3 corresponds to the insertion of a neutral oxygen atom (coming from the dissociation of O_2) into a vacancy. It expresses the fact that during the insertion of this oxygen atom, two electron holes are created (or in the inverse process, that two electron holes are suppressed by the release of two electrons coming from the oxygen vacancy formation. Thus, the electron holes (positively charged) compensate the negative charge associated to the substitution of La^{3+} by Sr^{2+} , in the absence of twice positively charged oxygen vacancies. Eq. 4 corresponds to the creation of an electron-hole pair.

At thermodynamic equilibrium, the oxygen vacancy concentration is governed by the change in Gibbs free energy associated with the previous reactions:

$$\Delta G_{O_x}^o = \Delta H_{O_x}^o - T\Delta S_{O_x}^o = -RT\ln(K_{O_x} \{P_{O_2}\}), \quad (5)$$

$$\Delta G_i^o = \Delta H_i^o - T\Delta S_i^o = -RT\ln(K_i), \quad (6)$$

where G^o , ΔH^o , ΔS^o and K are the standard Gibbs free energy change, the standard enthalpy change, the standard entropy change and the equilibrium constants of the two reactions, respectively denoted by the subscripts o_x and i . Eq. 5 expresses the balance between the entropy variation when oxygen vacancy defects are introduced into the crystal and the enthalpy cost necessary to form these defects. Eq. 6 describes the Gibbs free energy change during the formation of a $Fe'_{Fe}/Fe^{\bullet}_{Fe}$ pair.

Eqs. 5 and 6, together with the electroneutrality condition ($x + [Fe'_{Fe}] = 2\delta + [Fe^{\bullet}_{Fe}]$) and using the fact that the concentrations in the different Fe species in LSF sum to unity ($[Fe'_{Fe}] + [Fe^x_{Fe}] + [Fe^{\bullet}_{Fe}] = 1$), forms a set of equations equivalent to an equation of state (note that the concentrations of each species are expressed in number of moles for one mole of LSF). Solving this set of equations for any partial oxygen pressure and temperature gives the defect concentrations. The set of equations are solved using the least square method.

In this work, the standard enthalpy change during the formation of a $Fe'_{Fe}/Fe^{\bullet}_{Fe}$ pair is approximated by taking the difference between the conduction band minimum E_{CB} and the valence band maximum E_{VB} :

$$\Delta H_i^{o,DFT} \approx E_{CB} - E_{VB} = E_g \quad (7)$$

On the other hand, the standard enthalpy change $\Delta H_{O_x}^o$ during oxygen vacancy formation is approximated as minus the formation energy of the oxygen vacancy at T=0 K, as obtained from our GGA+ U calculations:

$$\Delta H_{O_x}^{o,DFT} \approx -E_f, \quad (8)$$

for which we choose the smallest calculated value ($E_f=0.871$ eV for $x \approx 0.1$, and 0.809 eV for $x \approx 0.4$).

Note that both the standard enthalpy change from Mizusaki *et al.* and the DFT calculated one are assumed to depend neither on the temperature (Ellingham approximation) nor on the oxygen vacancy concentration. This assumption can be justified since the experimentally measured data were in very good agreement with the defect model in the studied temperature range between 700 °C and 1200 °C. Furthermore, Ritzman *et al.* [25] found that the thermal and vibrational corrections to the standard enthalpy change is rather negligible (around 0.03 eV at 700 °C). As including thermal and vibrational corrections to the enthalpy would need cost-intensive phonon calculations, the corresponding contributions are neglected, and thus not considered, in the present study.

In Fig. 13 (a) the oxygen concentration $3 - \delta$ is plotted as a function of oxygen partial pressure P_{O_2} at 1073 K for a strontium content of $x \approx 0.4$ (δ is the oxygen vacancy concentration). Mizusaki *et al.* extracted the values of $\Delta H_{O_x}^o$, $\Delta S_{O_x}^o$, ΔH_i^o , ΔS_i^o from the experimental evolution δ with P_{O_2} measured by thermogravimetric analysis (TGA). They observed that the dependency of $\Delta H_{O_x}^o$, $\Delta S_{O_x}^o$ and ΔS_i^o on x is almost negligible, while ΔH_i^o was found to change significantly with the Sr content x .⁶⁰ The values of their extracted enthalpies and entropies at $x=0.4$ equal $\Delta H_{O_x}^o=-23.6$ kcal/mol, $\Delta H_i^o=30.45$ kcal/mol, $\Delta S_{O_x}^o=-15.62$ cal/K mol and $\Delta S_i^o=-0.96$ cal/K mol.⁵⁹

To plot the DFT curve in Fig. 13 a), the standard enthalpy change $\Delta H_{O_x}^o$ was determined using the calculated energy of oxygen vacancy formation at the most favorable site was (cf Eq. 8, $\Delta H_{O_x}^{o,DFT}=-0.809$ eV=-18.7 kcal/mol) while $\Delta H_i^{o,DFT}$ equals 1.46 eV=33.6 kcal/mol (Tab. VIII). It can be noted that, the entropy calculation is above the scope of this work because it is not trivial and cost-intensive with DFT since it includes a vibrational

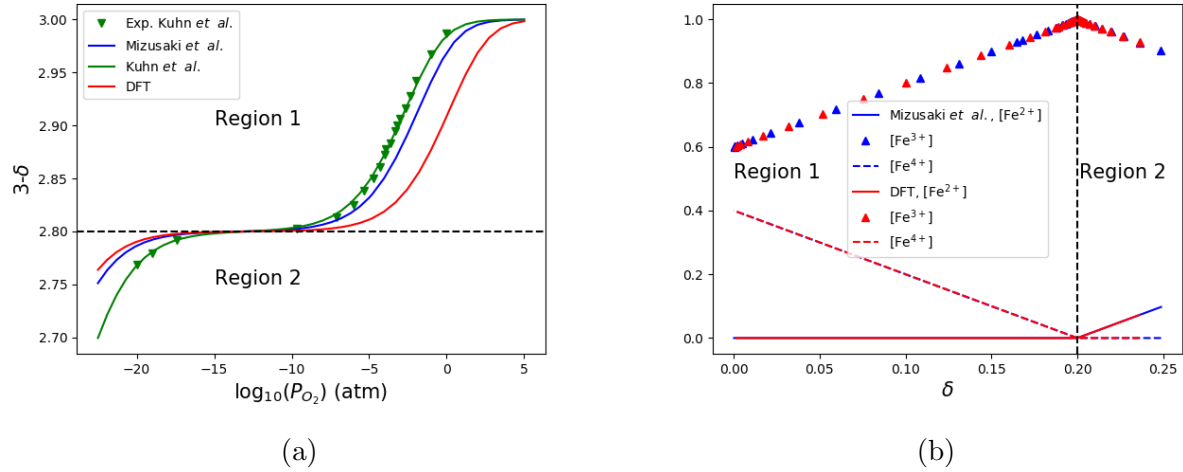


FIG. 13: (a) Oxygen concentration ($3-\delta$) as a function of oxygen partial pressure P_{O_2} and (b) concentrations of irons in different oxidation states as a function of oxygen nonstoichiometry at 1073 K for $x \approx 0.4$.

contribution in addition to the configurational one. Therefore, for the DFT plots in Fig. 13, the experimentally derived entropy changes were used. The experimental and DFT obtained oxygen vacancy concentrations as a function of P_{O_2} can be interpreted by separating them into two regions.

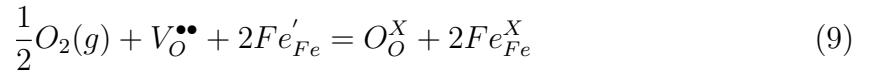
- Region 1:

At high oxygen partial pressure, the oxygen vacancy formation is not favored. In this condition ($\delta = 0$), the ionic charge difference created by the substitution of La^{3+} with Sr^{2+} is totally compensated by the formation of electron holes. As previously highlighted, the electron holes are localized within the band gap and are associated to Fe^{4+} ions (see Fig. 13 (b)). Therefore, the concentration of Fe^{4+} equals exactly the Sr concentration x . With decreasing oxygen partial pressure, vacancy formation becomes more and more favorable. According to the reaction given in Eq. 3, the two liberated electrons coming from the oxygen vacancy formation are redistributed on two Fe^{4+} , thus neutralizing the two holes, and reducing back these two Fe^{4+} into Fe^{3+} . In the first region, therefore, the concentration of $[Fe^{4+}]$ and $[Fe^{3+}]$ decreases and increases respectively, with the same slope, until reaching the inflection point of the defect diagram, which corresponds to the case $\delta=x/2=0.2$ (Fig. 13). At this

point, all localized electron hole states, that lay within the band gap, have been filled: there is no more Fe^{4+} , while the concentration of $[\text{Fe}^{3+}]$ reaches its upper bound. The charge compensation of the Sr dopants is then fully ensured by doubly charged oxygen vacancies.

- Region 2:

Decreasing further the oxygen partial pressure can lead to the creation of more oxygen vacancies by reducing the iron charge from Fe^{3+} to Fe^{2+} according to the following reaction:



Therefore, in region 2, the concentration of Fe^{3+} decreases while the concentration of Fe^{2+} increases (and that of Fe^{4+} remains at zero).

In the article of Mizusaki *et al.* (Ref. [60]), the experimental data for the oxygen nonstoichiometry is not available for $x \approx 0.4$, only the extracted standard enthalpy and entropy values, leading together with the defect model to the blue curve in Fig. 13 (a), are given. Therefore, additionally the thermogravimetry and coulometric titration measurement data points of Kuhn *et al.* have been extracted for comparison from the Fig. 4. a) in Ref. [61] (cf. green triangles in Fig. 13 (a)). Kuhn *et al.* fitted parameters for the defect model on these data points, leading to the green curve in Fig. 13 (a). It can be observed that the DFT curves in Fig. 13 are in satisfying agreement with the experimental data points and the defect models based on experimentally derived parameters. Even though we did not perform any direct DFT calculation corresponding to the region 2. (i.e. $\delta > x/2$), in this region the DFT based defect model (red curve) is in surprising good agreement with the defect model of Mizusaki *et al.* (blue curve). In fact, the enthalpy change, ΔH_i^o , associated with the formation of the $Fe'_{\text{Fe}}/Fe^{\bullet}_{\text{Fe}}$ pair is in excellent agreement with the experimental value. In Tab. VIII, it can be observed that ΔH_i^o decreases with the decreasing unit cell volume which is in turn correlated with the strontium concentration.

In Tab. IX previously reported DFT determined formation energies and enthalpies are listed. The GGA calculations carried out by Mastrikov *et al.* with a ferromagnetic order, give rise to high oxygen vacancy formation energies (3.39-3.60 eV) compared to experiment.

TABLE VIII: DFT derived ΔH_i^o values at different Sr concentrations in eV and kcal/moles, as well as the volume per 5-atom unit cell

x	$\Delta H_i^{o,DFT}$ [eV]	$\Delta H_i^{o,DFT}$ [kcal/mole]	V [\AA^3]
0.0	2.04	47.1	60.7
0.1	1.92	44.2	60.4
0.4	1.46	33.6	59.2
0.6	1.05	24.2	58.4

In table IX, it can be noticed that DFT+ U calculations result in lower oxygen vacancy formation energies. In the DFT+ U calculations of Ritzman *et al.*, holes are mainly delocalized over the oxygen sublattice and compensated during oxygen vacancy formation, while according to the authors the oxidation state of Fe remains unchanged to 3+. The oxygen vacancy formation energy in the 160 atom supercell are underestimated by 1.1 eV, 0.88 eV et 0.72 eV for $x=0.0$, $x=0.25$, and $x=0.5$, respectively. They partially attribute the underestimation to the overbinding of the O_2 molecule in DFT-GGA, but which can not fully explain the discrepancy. The hybrid PBE0 and GGA+ U calculations by Gryaznov *et al.* in a ferromagnetic order give rise to oxygen vacancy formation energies between 0.54 eV and 2.37 eV depending on the functional and the vacancy to strontium ratio. In the present calculations using the experimentally observed antiferromagnetic order, the correct physical mechanism of oxygen vacancy formation, which is associated to the change in Fe oxidation state, is reproduced and the mean oxygen vacancy formation energy is close to the experimental value of around 1.1 eV.

C. Oxygen concentration as a function of P_{O_2} and Sr-content ($x = 0.0, x \approx 0.1, 0.4, 0.6$)

The set of equations given by Mizusaki *et al.* (cf. section VB) are valid for Sr concentrations $x \neq 0$. Therefore, for pure LaFeO_3 the previous set of equations can not be used. In the case of pure LaFeO_3 ($x=0$) the reaction that describes the oxygen vacancy formation is expressed as follows:

TABLE IX: DFT determined (T=0 K) and high-temperature values for formation energies and enthalpies (in eV) for different strontium contents x and defect concentrations δ .

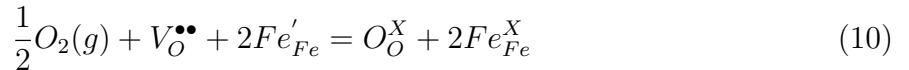
x	method	δ	$-\Delta H_{Ox}^{min/max}$	$-\Delta H_{Ox}^{mean}$	T [K]
0.125	PBE0 ⁵⁵ d)	0.0625	0.54/1.09		1200
0.125	PBE0 ⁵⁵ c)	0.125	2.08/2.37		1200
0.50	PBE0 ⁵⁵ c)	0.125	0.04/0.27		1200
0.50	PBE U=4.5 ⁵⁵ c)	0.125	1.78/1.91		1200
0.50	PBE U=6.5 ⁵⁵ c)	0.125	1.32/1.44		1200
0.25	PBE U=4.3 ²⁵ a)	0.125		0.69 ± 0.17	700
0.25	PBE U=4.3 ²⁵ b)	0.031		0.12	700
0.50	PBE U=4.3 ²⁵ a)	0.125		-0.01 ± 0.28	700
0.50	PBE U=4.3 ²⁵ b)	0.031		0.28	700
x	method	δ	$E_f^{min/max}$	E_f^{mean}	
0.25	PBE U=4.3 ²⁵ a)	0.125		0.71 ± 0.17	
0.25	PBE U=4.3 ²⁵ b)	0.031		0.14	
0.50	PBE U=4.3 ²⁵ a)	0.125		0.02 ± 0.28	
0.50	PBE U=4.3 ²⁵ b)	0.031		0.31	
0.50	GGA ⁶²	0.125	3.39/3.60		
0.09375	present	0.031	0.871/1.347	1.08	
0.375	present	0.042	0.809/1.343	1.035	

a) Pseudocubic (40-Atom) Supercell

b) SQS (160-Atom) Supercell

c) Rhombohedral (40-Atom) Supercell

d) Rhombohedral (80-Atom) Supercell



The enthalpy and entropy change associated to this reaction are ΔH° and ΔS° , respectively. Equation 10 is the same equation valid in the second region (i.e. $\delta > \frac{x}{2}$) for Sr concentrations $x \neq 0$ (cf. eq. 9). Thus by combining the equations 3 and 4, we can calculate the enthalpy and entropy change of eq. 10 as a function of the enthalpy and entropy changes

of reactions 3 and 4, such that $\Delta H^o = \Delta H_{ox}^o - 2\Delta H_i^o$ and $\Delta S^o = \Delta S_{ox}^o - 2\Delta S_i^o$. Now it is possible to use the experimentally derived values of ΔH_{ox}^o and ΔH_i for $x=0.003$ of reference [59] to calculate ΔH^o which gives rise to a value of around -5. eV. Comparing this value to the calculated DFT value in pure LaFeO_3 (i.e. -4.5 eV) leads to a satisfying agreement. Then using the reduced set of equation associated to reaction 10 (depending only on two parameters ΔH^o and ΔS^o), the oxygen content $3 - \delta$ as a function of partial pressure is calculated and given in Fig. 14. In the same figure the oxygen contents for $x \approx 0.1, 0.4, 0.6$ are given for comparison.

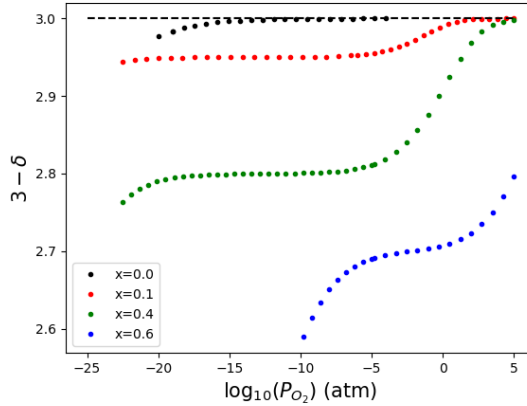


FIG. 14: Oxygen content $3-\delta$ as a function of partial oxygen pressure P_{O_2} for $x = 0$, $x \approx 0.1, 0.4$ and 0.6 at 1073 K

As previously described the P_{O_2} dependency for $x \neq 0$ can be divided into two regions, (i.e. $\delta > \frac{x}{2}$ and $\delta < \frac{x}{2}$), leading to the characteristic shape of the curve as described in section V B. The effect of Sr-concentration on the oxygen vacancy concentration can clearly be observed. While for pure LaFeO_3 the compound is stoichiometric at the oxygen partial pressure in air, the oxygen deficiency increases with increasing Sr-content. As mentioned in the introduction, the concentration of oxygen vacancies plays a key role on the electrode efficiency. For high cell performances, a low polarization resistance is desired. As given in equation (1), the polarization resistance decreases with increasing oxygen vacancy concentration. However, the increase in performance due to an increase in oxygen vacancy concentration is limited by several coexisting mechanisms, such as a phase decomposition which occurs at an oxygen deficiency of around $\delta = 0.23$ for $x=0.4$.⁶¹ As will be shown in the next section, the electronic conductivity governed by a polaron hopping process depends on the concentration of holes,

which, however, decreases by increasing oxygen vacancy concentration, at a given Sr concentration. Nevertheless, electronic conductivity is also important, thus under given experimental condition optimal balance between both should be found, but which is beyond the scope of this work.

D. Conduction properties

In the previous section, the defect concentrations as a function of temperature and oxygen partial pressure have been determined, in particular the hole concentration $[h]$ (which equals the Fe^{4+} concentration). In this section, we aim to describe the hole conductivity as a function of temperature and oxygen partial pressure. Making the approximation that hole diffusion is isotropic, the hole conductivity σ_h is given by

$$\sigma_h = e[h]\mu_h, \quad (11)$$

where e and μ_h denote respectively the elementary electronic charge (positive value) and the hole mobility. The latter is related to the hole diffusion coefficient D_h by

$$\mu_h = \frac{eD_h}{k_B T} \quad (12)$$

In LSF, holes were found to localize under the form of polarons (we will consider here that the theory describing small polarons in crystals applies to the present holes, even if they are not strictly localized on a single atom). In insulating compounds, small polarons result from the localization of an elementary charge (electron or hole) due to *self-trapping*: in this phenomenon, the localization of the charge on an atom creates all around a radial polarization field, which in turn generates on the considered site an additional electrostatic potential, which is favorable to the localization of the charge. If the polaronic state is stable, the resulting electrostatic coupling (between the charge and the polarized matrix) compensates other energy costs associated to the process, in particular the zero-point energy associated with the quantum confinement of the charge. The set of atomic displacements that necessarily accompanies the localization is called the "self-trapping distortion", and both (atomic distortions + localized charge) form the small polaron. The resulting lattice configuration is called the self-trapping configuration. In this case, the potential which is

undergone by the charge (electronic potential), has a pronounced minimum at the site where the charge is localized.

Small polaron transport proceeds by successive hoppings, and is a thermally activated process: the activation energy corresponds to the energy cost to bring the system from its stable self-trapped polaronic (self-trapping) configuration, the lowest-energy lattice configuration in which the electronic potential is a symmetric double well, with the two ground levels in coincidence. This so called "coincidence configuration"⁶³ can be approximated by the configuration having the highest energy along the hopping paths displayed on Fig. 5. Its energy with respect to the self-trapped one is called the coincidence energy E_c : it plays the role of the activation energy for the small polaron hopping process. In the coincidence configuration, the charge tunnels through the electronic barrier with a typical time $\approx \hbar/2C$, C being the electronic coupling in this configuration. Along the hopping path, the self-trapping distortion is progressively transferred from the initial site onto the final one. The energy barrier is paid by the thermal agitation of the surrounding atoms – which may be considered as classical particles – and not by the charge itself, which behaves quantum-mechanically and remains in its ground state all along the hopping.

The diffusion coefficient in Eq. 12 is related to the hole hopping rate k_h by

$$D_h = ga^2k_h, \quad (13)$$

where a is the hopping distance and g is a geometrical factor.

There are two limiting regimes for small polaron hopping:

- if the tunneling time is short with respect to the time scale of the coincidence, the charge automatically transfers by tunneling at each coincidence event, and the polaron transfer is qualified as *adiabatic*. The hopping rate k_h is then controlled by the vibrations of the host lattice,

$$k_h = k_{phon}e^{-\frac{E_c}{k_B T}}, \quad (14)$$

where k_{phon} is the frequency of the typical phonon mode along which the system evolves from the self-trapped configuration to the coincidence one. Thus, in the adiabatic limit the hole conductivity becomes:

$$\sigma_h = \frac{e^2[h]}{(k_B T)} g a^2 k_{phon} e^{-\frac{E_c}{k_B T}} \quad (15)$$

The term $\sigma_h.T$ has thus the Arrhenius form, with the coincidence energy playing the role of the activation energy, and the pre-factor controlled by the host vibrations.

- if the tunneling time is large with respect to the time scale of the coincidence, the charge has not the time to transfer by tunneling at each coincidence event: it only transfers with a small probability, and the polaron transfer, if any, is then qualified to be *non-adiabatic*. The hopping rate is then controlled by the quantum behavior of the charge in the electronic potential at coincidence, and is given by the Flynn-Stoneham formula

$$k_h = \frac{1}{2\hbar} \left(\frac{\pi}{E_c k_B T} \right)^{\frac{1}{2}} C^2 e^{-\frac{E_c}{k_B T}}. \quad (16)$$

The hole conductivity in this non-adiabatic limit is then given by:

$$\sigma_h = \frac{e^2[h]}{(k_B T)^{\frac{3}{2}}} \cdot \frac{1}{2\hbar} \left(\frac{\pi}{E_c} \right)^{\frac{1}{2}} C^2 g a^2 e^{-\frac{E_c}{k_B T}} \quad (17)$$

The coincidence energy plays also here the role of the activation energy but the prefactor of $(\sigma_h.T)$ includes a slight temperature dependence (proportional to $1/(T^{1/2})$), and is related, via the electronic coupling C , to the quantum character of the hole that tunnels through the electronic barrier at coincidence, with a small probability.

The Landau-Zener (LZ) thermal parameter γ_{th} may help to determine whether the hopping is adiabatic or not

$$\gamma_{th} = \frac{2\pi}{\hbar\omega_{phon}} \left(\frac{\pi}{E_s k_B T} \right)^{1/2} C^2 \quad (18)$$

with $E_s \approx 4E_c$ being the reorganization energy. $\gamma_{th} \gg 1$ corresponds to the adiabatic limit, while $\gamma_{th} \ll 1$ corresponds to the non-adiabatic one.

Knowing that the coincidence energy E_c can be approximated from the previous DFT computation. The missing quantity to describe the hole conductivity in Eqs. 15 and 17 are the phonon frequency k_{phon} and the electronic coupling constant C , depending on the hopping mechanism. In the adiabatic limit, the phonon frequency can be in theory calculated

by performing DFT phonon calculations. As these calculations are cost-intensive, they have not been performed in the present study. Nevertheless, the phonon frequency and coupling constant are fitted on experimental conductivity data and then the Landau-Zener (LZ) thermal parameter is calculated in order to determine the type of hopping mechanism. The experimental conductivity of LSF (for $x=0.1$) from Braun *et al.* is used and the fitting is done at a sufficiently low temperature range to neglect the temperature dependence of the prefactor of $\sigma_h \cdot T$, i.e. $T=300-400$ K. At this temperature and considering the atmospheric condition (i.e. P_{O_2}), the hole concentration is equal the strontium concentration according to the defect model. As previously discussed, the activation energies calculated by DFT constitute an upper limit for the real activation energy. Therefore, the lowest calculated activation energy is used and round down to one decimal place, i.e. $E_c = 0.3$ eV, for the present analysis. Supposing an adiabatic hopping mechanism, the fit leads to a phonon frequency of around $4.6/g$ THz, which is consistent with the expected order of magnitude for a phonon frequency. When supposing a non-adiabatic mechanism, a high and unphysical electronic coupling constant of around $1700/\sqrt{g}$ eV is found. This value leads to a LZ thermal parameter much higher than the one ($\gamma_{th} \gg 1$), in contradiction with the assumption of non-adiabaticity. Consequently, this analysis suggests that the hopping mechanism would be mainly controlled by the so-called adiabatic process depicted by Eq. 15. It can be noted that this statement strengthens the claim of some authors who have assumed that the polaron transfer is controlled by an adiabatic mechanism.^{51,49}

In the adiabatic limit, the dependence with the oxygen partial pressure of the hole conductivity in LSF ($x=0.1$) has been calculated for different temperatures (Fig. 15 (a)). For this purpose, the thermodynamic defect model associated with the DFT enthalpies, the DFT activation energy and the fitted phonon frequency have been combined. In Fig. 15 (a), the calculated conductivities follow the evolution of the defect concentration in region 1 (cf. Fig. 13 (a)), as the creation of oxygen vacancy is accompanied by the compensation of holes through the reduction of Fe^{4+} into Fe^{3+} (Eq. 3). It can be observed that, in the upper range of the oxygen partial pressure, the conductivity increases with temperature. In contrast, when lowering the oxygen partial pressure, the curvature of the curves is changed and the temperature dependence is reversed. This modification can be mainly ascribed to the faster decrease of the hole concentration with increasing temperatures. Plotting the hole conductivity as a function of hole concentration (Fig 13 (b)) shows a linear dependence on

the hole concentration (Eq. 11). Furthermore, for each hole concentration the conductivity increases with temperature due to the thermal activation given by the exponential term in Eq. 15.

As the phonon frequency was fitted on the data from Braun *et al.* [47], the calculated hole conductivity at 482 K is in good agreement with the latter. The conductivity measured at 483 K by Wang *et al.* lie above but remains coherent with the calculations. However, the calculated conductivity values at higher temperatures deviates from the experimental values of Mizusaki *et al.* at 1173.15 K.⁶⁴ Please note that besides the experimental conditions under which measurement are carried out, the microstructural properties of the sample might influence the conductivity

As discussed in Sec. III C 2, the experimental activation energy was found to decrease at a higher temperature range. Therefore, in Fig. 15 (c) and (d), hole conductivity is calculated using a lower activation energy (i.e. 0.1 eV). As expected with this value, the conductivity is substantially increased (Fig. 15 (c)). In the studied temperature range, whatever the investigated oxygen partial pressure, the hole conductivity is found to decrease with increasing temperature. In contrast to the conductivities calculated with an activation energy of 0.3 eV, it is shown in Fig. 15 (d) that the conductivity at a given hole concentration becomes nearly temperature independent and even decreases slightly with temperature. This evolution has also been observed in the experimental study published by S \o gaard *et al.* in the case of $x \approx 0.4$.⁶⁵ The authors were surprised by the lack of thermal activation of the electrical conduction with the temperature at a constant charge carrier concentration which they supposed to be in contradiction with a small polaron conductor. However, this counter-intuitive dependence with temperature can result from the mathematical expression of hole polaron conductivity (Eq. 15). Indeed, the conductivity first increases with temperature due to the exponential term, reaches a maximum at $E_c = k_B T$ and then decreases due to the prefactor term with a $1/T$ -dependence. In the temperature range between 1173.15 K and 1573.15 K for $E_c = 0.3$ eV the exponential term predominates ($k_B T < E_c$), while $k_B T \approx E_c$ for $E_c = 0.1$ eV.

From this analysis, it can be thus reasonably proposed that the activation energy for the hole conductivity changes from 0.3 eV below the N \e el temperature (around 600 K) to 0.1 eV at higher temperatures where polaron hopping between nearest neighbours might become possible.

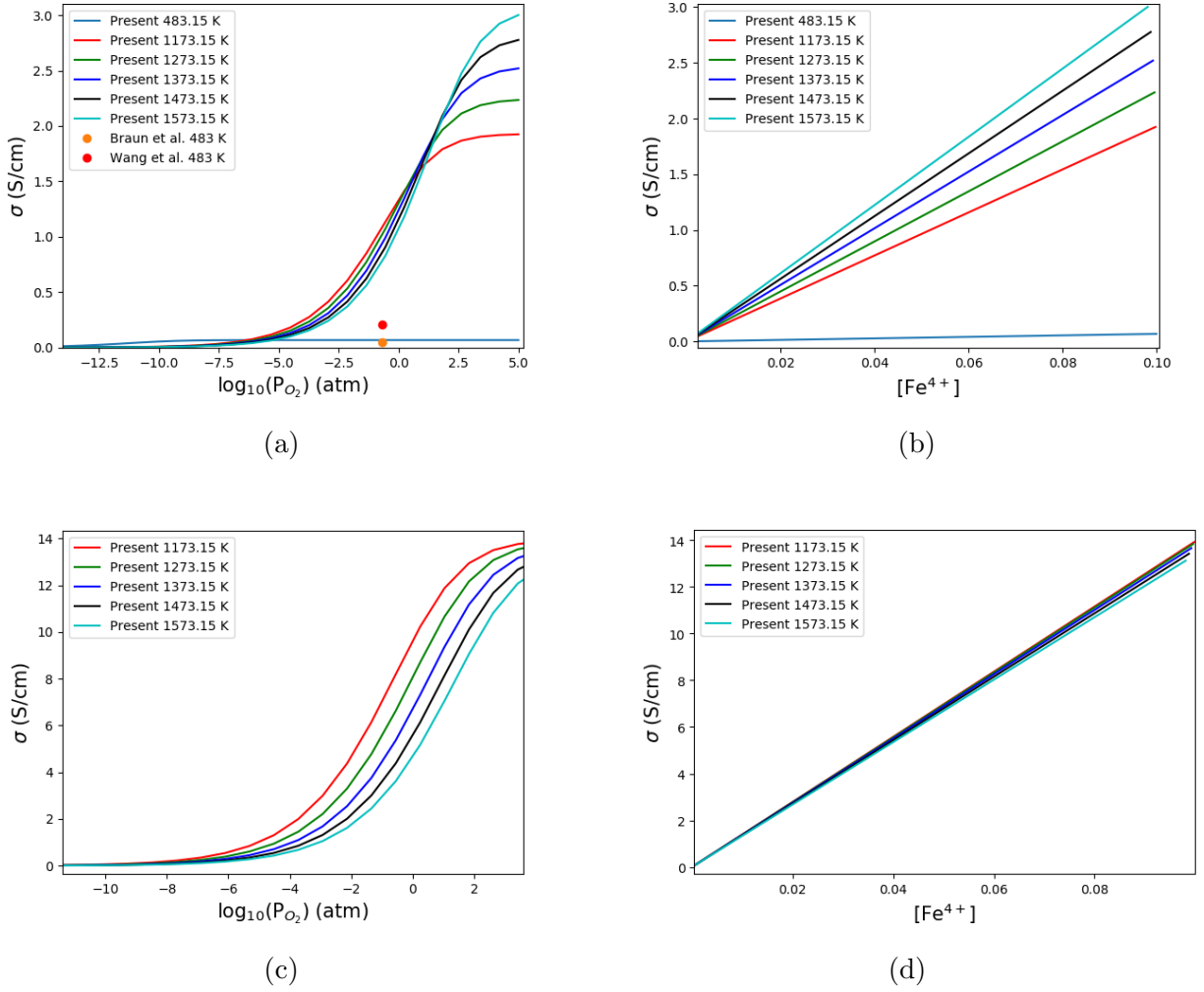


FIG. 15: Hole conductivity as a function of partial oxygen pressure and as a function of hole concentration. (a), (b): $E_c = 0.3$ eV. (c), (d): $E_c = 0.1$ eV.

The present study about hole conductivity has been restricted to the low Sr-concentration ($x=0.1$). At higher Sr-concentration, the site-blocking effect due to the presence of other holes (i.e. the probability that the adjacent site onto which the polaron hops may already be occupied) might to be taken into account.⁶⁶ Furthermore, the oxygen vacancy concentration is increased for higher Sr concentration and should reduce the number of available hopping sites.⁶⁵ In this condition, it is not trivial to derive an accurate mathematical expression that could include these additional effects in the hole conductivity.

VI. CONCLUSION

In this work, we have studied, by Density Functional Theory+ U and hybrid density-functional calculations, the electron holes in pure LaFeO_3 , and the effect of the presence of Sr impurities in $\text{La}_{1-x}\text{Sr}_x\text{FeO}_3$. The holes are found to localize under a polaronic form in LaFeO_3 , with the corresponding quantum state extending over one Fe atom and four neighboring oxygen. The energy barriers associated with the hopping of this hole polaron are around 0.3-0.4 eV. In the presence of Sr impurities (Sr substituting La), the holes are localized, with the Sr impurities probably acting as shallow traps. The oxygen vacancies have been studied for $x \approx 0.1$ and 0.4. The formation energies are positive and found around 0.8 eV in the most favorable sites. The DFT values have been used to feed a defect model that describes how the defect concentration evolves with oxygen partial pressure and temperature. Furthermore, the hole conductivity has been investigated as a function of the oxygen pressure and for different temperatures.

ACKNOWLEDGEMENTS

This work was granted access to the HPC resources of TGCC under the allocation 2020-[A0100911394] made by GENCI. This project has received funding from the Fuel Cells and Hydrogen 2 Joint Undertaking (JU) under grant agreement n° 874577 (NewSOC project). The JU receives support from the European Union's Horizon 2020 research and innovation program and Denmark, France, Italy, Spain, Poland, Netherlands, Greece, Finland, Estonia, Germany, United Kingdom, Switzerland. The work has also been partially supported by the PTC simulation program at CEA (SOLSTIS project) and Genvia company. The authors would like to express their thanks to Maxime Hubert, Elisa Effori, Lea Rorato and Guiseppe Sassone for interesting discussions.

* cintia.hartmann@cea.fr

† gregory.geneste@cea.fr

¹ S. P. Jiang, International Journal of Hydrogen Energy **44**, 7448 (2019).

- ² K. K. Hansen, *Solid State Ionics* **344**, 115096 (2020).
- ³ M. D. Scafetta, Y. J. Xie, M. Torres, J. E. Spanier, and S. J. May, *Appl. Phys. Lett.* **102**, 081904 (2013).
- ⁴ S. Y. Smolin, M. D. Scafetta, A. K. Choquette, M. Y. Sfeir, J. B. Baxter, and S. J. May, *Chem. Mat.* **28**, 97 (2016).
- ⁵ J. B. Yang, W. B. Yelon, W. J. James, Z. Chu, M. Kornecki, Y. X. Xie, X. D. Zhou, H. U. Anderson, and S. K. Joshi, A. G. Malik, *Physical Review B* **66**, 184415 (2002).
- ⁶ S. K. Park, T. Ishikawa, Y. Tokura, J. Q. Li, and Y. Matsui, *Physical Review B* **60**, 10788 (1999).
- ⁷ J. Ma, J.-Q. Yan, S. O. Diallo, R. Stevens, A. Llobet, F. Trouw, D. L. Abernathy, M. B. Stone, and R. J. McQueeney, *Physical Review B* **84**, 224115 (2011).
- ⁸ D. Sastre, D. P. Serrano, P. Pizarro, and J. M. Coronado, *Journal of CO2 Utilization* **31**, 16 (2019).
- ⁹ K. Zhao, F. He, Z. Huang, A. Zheng, H. Li, and Z. Zhao, *Chinese Journal of Catalysis* **35**, 1196 (2014).
- ¹⁰ D. D. Taylor, N. J. Schreiber, B. D. Levitas, W. Xu, P. S. Whitfield, and E. E. Rodriguez, *Chem. Mat.* **28**, 3951 (2016).
- ¹¹ Z. Shen, Y. Zhuang, W. Li, X. Huang, F. E. Oropeza, E. J. M. Hensen, J. P. Hofmann, M. Cui, A. Tadich, D. Qi, J. Cheng, J. Li, and K. H. L. Zhang, *J. Mater. Chem. A* **8**, 4407 (2020).
- ¹² L. Wang, Y. Du, P. V. Sushko, M. E. Bowden, K. A. Stoerzinger, S. M. Heald, M. D. Scafetta, T. C. Kaspar, and S. A. Chambers, *Phys. Rev. Materials* **3**, 025401 (2019).
- ¹³ Y. J. Xie, M. D. Scafetta, E. J. Moon, A. L. Krick, R. J. Sichel-Tissot, and S. J. May, *Appl. Phys. Lett.* **105**, 062110 (2014).
- ¹⁴ M. Abbate, F. M. F. de Groot, J. C. Fuggle, A. Fujimori, O. Strebel, F. Lopez, M. Domke, G. Kaindl, G. A. Sawatzky, M. Takano, Y. Takeda, H. Eisaki, and S. Uchida, *Physical Review B* **46**, 4511 (1992).
- ¹⁵ A. Chainani, M. Mathew, and D. D. Sarma, *Phys. Rev. B* **48**, 14818 (1993).
- ¹⁶ S. B. Adler, J. A. Lane, and B. C. H. Steele, *Journal of The Electrochemical Society* **143**, 3554 (1996).
- ¹⁷ J. Laurencin, M. Hubert, K. Couturier, T. L. Bihan, P. Cloetens, F. Lefebvre-Joud, and E. Siebert, *Electrochimica Acta* **174**, 1299 (2015).

- ¹⁸ E. Effori, J. Laurencin, E. D. R. Silva, M. Hubert, T. David, M. Petitjean, G. Geneste, L. Dessemond, and E. Siebert, *Journal of The Electrochemical Society* **168**, 044520 (2021).
- ¹⁹ J. Laurencin, M. Hubert, D. F. Sanchez, S. Pylypko, M. Morales, A. Morata, B. Morel, D. Montinaro, F. Lefebvre-Joud, and E. Siebert, *Electrochimica Acta* **241**, 459 (2017).
- ²⁰ X. Gonze, F. Jollet, F. Abreu Araujo, D. Adams, B. Amadon, T. Applencourt, C. Audouze, J.-M. Beuken, J. Bieder, A. Bokhanchuk, E. Bousquet, F. Bruneval, D. Caliste, M. Côté, F. Dahm, F. Da Pieve, M. Delaveau, M. Di Gennaro, B. Dorado, C. Espejo, G. Geneste, L. Genovese, A. Gerossier, M. Giantomassi, Y. Gillet, D. Hamann, L. He, G. Jomard, J. Laflamme Janssen, S. Le Roux, A. Levitt, A. Lherbier, F. Liu, I. Lukačević, A. Martin, C. Martins, M. Oliveira, S. Poncé, Y. Pouillon, T. Rangel, G.-M. Rignanese, A. Romero, B. Rousseau, O. Rubel, A. Shukri, M. Stankovski, M. Torrent, M. Van Setten, B. Van Troeye, M. Verstraete, D. Waroquiers, J. Wiktor, B. Xu, A. Zhou, and J. Zwanziger, *Computer Physics Communications* **205**, 106 (2016).
- ²¹ J. P. Perdew, K. Burke, and M. Ernzerhof, *Phys. Rev. Lett.* **77**, 3865 (1996).
- ²² P. Blochl, *Physical Review B* **50**, 17953 (1994).
- ²³ M. Torrent, F. Jollet, F. Bottin, G. Zérah, and X. Gonze, *Computational Materials Science* **42**, 337 (2008).
- ²⁴ F. Jollet, M. Torrent, and N. Holzwarth, *Computer Physics Communications* **185**, 1246 (2014).
- ²⁵ A. M. Ritzmann, A. B. Muñoz-García, M. Pavone, J. A. Keith, and E. A. Carter, *Chemistry of Materials* **25**, 3011 (2013), <https://doi.org/10.1021/cm401052w>.
- ²⁶ A. M. Ritzmann, J. M. Dieterich, and E. A. Carter, *Phys. Chem. Chem. Phys.* **18**, 12260 (2016).
- ²⁷ T. Das, *Understanding Oxygen Vacancy Formation, Interaction, Transport, and Strain in SOFC Components via Combined Thermodynamics and First Principles Calculations*, Ph.D. thesis, Michigan State University (2017).
- ²⁸ S. Dann, D. Currie, M. Weller, M. Thomas, and A. Al-Rawwas, *Journal of Solid State Chemistry* **109**, 134 (1994).
- ²⁹ W. Koehler and E. Wollan, *Journal of Physics and Chemistry of Solids* **2**, 100 (1957).
- ³⁰ T. Arima, Y. Tokura, and J. B. Torrance, *Phys. Rev. B* **48**, 17006 (1993).
- ³¹ A. Zunger, S.-H. Wei, L. G. Ferreira, and J. E. Bernard, *Phys. Rev. Lett.* **65**, 353 (1990).
- ³² A. van de Walle, M. Asta, and G. Ceder, *Calphad* **26**, 539 (2002).

- ³³ J. J. Carey, J. A. Quirk, and K. P. McKenna, *The Journal of Physical Chemistry C* **125**, 12441 (2021), pMID: 34276864, <https://doi.org/10.1021/acs.jpcc.1c03136>.
- ³⁴ L. Bjaalie, D. G. Ouellette, P. Moetakef, T. A. Cain, A. Janotti, B. Himmetoglu, S. J. Allen, S. Stemmer, and C. G. Van de Walle, *Applied Physics Letters* **106**, 232103 (2015), <https://doi.org/10.1063/1.4922316>.
- ³⁵ A. Janotti, J. B. Varley, M. Choi, and C. G. Van de Walle, *Phys. Rev. B* **90**, 085202 (2014).
- ³⁶ L. Bjaalie, A. Janotti, K. Krishnaswamy, and C. G. Van de Walle, *Phys. Rev. B* **93**, 115316 (2016).
- ³⁷ B. Himmetoglu, A. Janotti, L. Bjaalie, and C. G. Van de Walle, *Phys. Rev. B* **90**, 161102 (2014).
- ³⁸ L. Weston, A. Janotti, X. Y. Cui, C. Stampfl, and C. G. Van de Walle, *Phys. Chem. Chem. Phys.* **19**, 11485 (2017).
- ³⁹ Y. K. Frodason, K. M. Johansen, T. S. Bjørheim, B. G. Svensson, and A. Alkauskas, *Phys. Rev. B* **95**, 094105 (2017).
- ⁴⁰ J. Heyd, G. E. Scuseria, and M. Ernzerhof, *J. Chem. Phys.* **118**, 8207. (2003).
- ⁴¹ J. Heyd, J. E. Peralta, G. E. Scuseria, and R. L. Martin, *The Journal of Chemical Physics* **123**, 174101 (2005).
- ⁴² G. Kresse and J. Furthmuller, *Phys. Rev. B: Condens. Matter* **54**, 11169–11186 (1996).
- ⁴³ Z. Zhu, H. Peelaers, and C. G. Van de Walle, *Journal of Materials Chemistry A* **5**, 15367 (2017).
- ⁴⁴ M. D. Scafetta, A. M. Cordi, J. M. Rondinelli, and S. J. May, *Journal of Physics: Condensed Matter* **26**, 505502 (2014).
- ⁴⁵ Q. Liu, *Synthesis, characterization and investigation on the magnetic and electronic structure of strontium iron oxides*, Ph.D. thesis, Université Sciences et Technologies - Bordeaux I (2013).
- ⁴⁶ G. P. Wheeler, B. V. U., T. J. Smart, A. Radmilovic, Y. Ping, and K.-S. Choi, *Chem. Mat.* **31**, 5890 (2019).
- ⁴⁷ A. Braun, J. Richter, A. S. Harvey, S. Erat, A. Infortuna, A. Frei, E. Pomjakushina, B. S. Mun, P. Holtappels, U. Vogt, K. Conder, L. J. Gauckler, and T. Graule, *Applied Physics Letters* **93**, 262103 (2008), <https://doi.org/10.1063/1.3049614>.
- ⁴⁸ W.-H. Jung, *Physica B: Condensed Matter* **299**, 120 (2001).
- ⁴⁹ H. Wang, C. Wang, J. Zhang, W. Su, J. Liu, M. Zhao, N. Yin, Y. Lv, and L. Mei, *Current Applied Physics* **10**, 866 (2010).

- ⁵⁰ K. KOBAYASHI, S. YAMAGUCHI, T. HIGUCHI, S. SHIN, T. TSUKAMOTO, and T. TSUNODA, *Electrochemistry* **72**, 870 (2004).
- ⁵¹ L.-W. Tai, M. Nasrallah, H. Anderson, D. Sparlin, and S. Sehlin, *Solid State Ionics* **76**, 259 (1995).
- ⁵² M. Patrakeev, I. Leonidov, V. Kozhevnikov, and K. Poeppelmeier, *Journal of Solid State Chemistry* **178**, 921 (2005).
- ⁵³ U. Shimony and J. M. Knudsen, *Phys. Rev.* **144**, 361 (1966).
- ⁵⁴ J.-C. Grenier, N. Ea, M. Pouchard, and M. Abou-Sekkina, *Materials Research Bulletin* **19**, 1301 (1984).
- ⁵⁵ D. Gryaznov, S. Baumann, E. A. Kotomin, and R. Merkle, *The Journal of Physical Chemistry C* **118**, 29542 (2014), <https://doi.org/10.1021/jp509206k>.
- ⁵⁶ A. M. Ritzmann, Ph.D. (2016).
- ⁵⁷ T. Das, J. D. Nicholas, and Y. Qi, *J. Mater. Chem. A* **5**, 25031 (2017).
- ⁵⁸ H. Wadati, D. Kobayashi, H. Kumigashira, K. Okazaki, T. Mizokawa, A. Fujimori, K. Horiba, M. Oshima, N. Hamada, M. Lippmaa, M. Kawasaki, and H. Koinuma, *Phys. Rev. B* **71**, 035108 (2005).
- ⁵⁹ J. Mizusaki, M. Yoshihiro, S. Yamauchi, and K. Fueki, *Journal of Solid State Chemistry* **58**, 257 (1985).
- ⁶⁰ J. Mizusaki, M. Yoshihiro, S. Yamauchi, and K. Fueki, *Journal of Solid State Chemistry* **67**, 1 (1987).
- ⁶¹ M. Kuhn, S. Hashimoto, K. Sato, K. Yashiro, and J. Mizusaki, *Solid State Ionics* **195**, 7 (2011).
- ⁶² Y. A. Mastrikov, R. Merkle, E. A. Kotomin, M. M. Kuklja, and J. Maier, *Phys. Chem. Chem. Phys.* **15**, 911 (2013).
- ⁶³ A. Shluger and A. Stoneham, *J. Phys.: Condens. Matter* **5**, 3049 (1993).
- ⁶⁴ J. MIZUSAKI, T. SASAMOTO, W. R. CANNON, and H. K. BOWEN, *Journal of the American Ceramic Society* **66**, 247 (1983), <https://ceramics.onlinelibrary.wiley.com/doi/pdf/10.1111/j.1151-2916.1983.tb15707.x>.
- ⁶⁵ M. Sogaard, P. Vang Hendriksen, and M. Mogensen, *Journal of Solid State Chemistry* **180**, 1489 (2007).
- ⁶⁶ J. Song, D. Ning, and H. J. M. Bouwmeester, *Phys. Chem. Chem. Phys.* **22**, 11984 (2020).